A hybrid Rayleigh-Taylor-current-driven coupled instability in a magnetohydrodynamically collimated cylindrical plasma with lateral gravity

Xiang Zhai and Paul M. Bellan

Citation: Physics of Plasmas **23**, 032121 (2016); doi: 10.1063/1.4943896
View online: http://dx.doi.org/10.1063/1.4943896
View Table of Contents: http://scitation.aip.org/content/aip/journal/pop/23/3?ver=pdfcov
Published by the AIP Publishing

A hybrid Rayleigh-Taylor-current-driven coupled instability in a magnetohydrodynamically collimated cylindrical plasma with lateral gravity

Xiang Zhai[a] and Paul M. Bellan[b]
Applied Physics, Caltech, Pasadena, California 91125, USA

(Received 28 April 2015; accepted 18 February 2016; published online 22 March 2016)

We present an MHD theory of Rayleigh-Taylor instability on the surface of a magnetically confined cylindrical plasma flux rope in a lateral external gravity field. The Rayleigh-Taylor instability is found to couple to the classic current-driven instability, resulting in a new type of hybrid instability that cannot be described by either of the two instabilities alone. The lateral gravity breaks the axisymmetry of the system and couples all azimuthal modes together. The coupled instability, produced by combination of helical magnetic field, curvature of the cylindrical geometry, and lateral gravity, is fundamentally different from the classic magnetic Rayleigh-Taylor instability occurring at a two-dimensional planar interface. The theory successfully explains the lateral Rayleigh-Taylor instability observed in the Caltech plasma jet experiment [Moser and Bellan, Nature **482**, 379 (2012)]. Potential applications of the theory include magnetic controlled fusion, solar emerging flux, solar prominences, coronal mass ejections, and other space and astrophysical plasma processes. © *2016 AIP Publishing LLC*.
[http://dx.doi.org/10.1063/1.4943896]

I. INTRODUCTION

Rayleigh-Taylor (RT) instability is a well-known hydrodynamic instability occurring when a gravitational field points from a high density fluid to a low density fluid.[1–3] In the case that the low density fluid is vacuum and the interface is planar, the growth rate of the one-dimensional (1D) RT instability is

$$\gamma = \sqrt{gk}, \tag{1}$$

where g is the gravity and k is the spatial wavenumber of the perturbation on the interface. The instability grows as $\exp(\gamma t)$ in early time when the disturbance caused by the instability is small so that linear stability analysis is valid. The RT instability prefers small scale perturbations because larger k gives faster growth rate. Equation (1) results from assuming incompressible fluid with no surface tension. It is known that finite compressibility can stabilize long wavelength perturbations (small k) while surface tension suppresses short wavelength (large k) perturbations.[1] At later times, the RT instability is well known to develop bubble and finger-like structures that further undergo Kevin-Helmholtz instability.

The RT instability in a magnetized plasma was first considered by Kruskal and Schwarzschild.[4] For a plasma "sitting" above vacuum with a magnetic field parallel to the planar interface, magnetohydrodynamic (MHD) theory shows the growth rate of this two-dimensional (2D) magnetic Rayleigh-Taylor (MRT) instability is

$$\gamma^2 = gk - \frac{(\mathbf{k}\cdot\mathbf{B}_0)^2}{\mu_0\rho}, \tag{2}$$

where $\mathbf{B}_0$ is the unperturbed magnetic field, $\mathbf{k}$ is the perturbation wavevector, and ρ is the density of the plasma.[2–4] It is seen that finite $\mathbf{k}\cdot\mathbf{B}_0$ reduces the growth rate. Because the instability phase is $i\mathbf{k}\cdot\mathbf{x}$, the wavevector $\mathbf{k}$ is perpendicular to the direction of constant phase. This means that for perturbations that try to bend magnetic field lines, i.e., $\mathbf{k}$ not perpendicular to $\mathbf{B}_0$, the magnetic field has a stabilizing effect. In particular, Eq. (2) shows that a perturbation with $\mathbf{k} \parallel \mathbf{B}_0$ (often called undular mode) is completely suppressed by magnetic field line tension if $k > \mu_0\rho g/B_0^2$. For a perturbation with $\mathbf{k}\perp\mathbf{B}_0$, sometimes called the interchange mode, the instability is identical to the hydrodynamic case. However, finite shear in the magnetic field can make a perturbation impossible to align with magnetic field at all depths, and thus helps to stabilize the system.[2] The highly anisotropic nature of the MRT instability has motivated efforts to study its nonlinear behavior using three-dimensional (3D) numerical simulations. It is found that at later times a strong magnetic field may even enhance the growth of bubbles and fingers in comparison to a purely hydrodynamic instability.[5]

The RT and MRT instabilities occur in various situations and the "gravity" g can originate from different sources. In astrophysical situations such as accretion processes and supernovae remnants, the RT instability happens due to the centripetal gravity from the central object.[5] The interfaces are cylindrical or spherical surfaces. Magnetic implosion of metal liner or Z-pinch plasmas are subject to the MRT instability on the cylindrical interface with the effective gravity caused by radial acceleration of the interface.[6–9] In laser-based inertial confinement fusion and laser-produced plasma experiments, the RT instability happens when the

[a]xzhai@caltech.edu
[b]pbellan@caltech.edu

ablation fronts are accelerated by laser irradiation.[10,11] The Parker instability or magnetic buoyancy instability can occur when a horizontal magnetic field increasing with depth supports heavier gas on top.[12–15] This instability shares the same physics as the MRT instability. In space plasmas and magnetic confinement, a concept of "bad" curvature or "good" curvature of magnetic field is also related to the MRT instability. This is because curved magnetic field lines can introduce an effective gravity to the plasma, as a result of centrifugal force resulting from guiding center motion along curved field lines.[2] In magnetic confinement devices and space plasma, when a pressure gradient exists at a location where the magnetic field has an unfavored curvature, the configuration is RT unstable, and gives rise to the ballooning mode.[16–18] These RT and MRT processes, despite their diverse geometries and causes, share a common feature that the (effective) gravity **g** is perpendicular to the interface. In this sense, the interfaces can be approximately treated as planar.

A recent lab experiment by Moser and Bellan showed a Rayleigh-Taylor instability developed on one side of a cylindrical argon plasma jet.[20] In the experiment, a plasma jet is created and collimated to a uniform radius of 2–5 cm by MHD forces. The plasma inside the jet is singly ionized with an estimated electron density $n_e \approx 10^{21} - 10^{22}\,\mathrm{m}^{-3}$. Outside the jet is weakly ionized plasma with negligible density and pressure. The cylindrical jet carries a strong axial magnetic field of 0.2–0.6 T and a large axial current of 50–150 kA, so the magnetic field is in a typical flux rope configuration.[19,21,22] When the jet is sufficiently long, it undergoes an $m = -1$ kink instability.[23] The kinked plasma grows nonlinearly fast and accelerates laterally away from the original central jet axis. In the plasma frame, an equivalent gravity is created due to the acceleration, pointing laterally from the plasma, which is a heavy gas, to the center axis, which is now nearly vacuum. The lateral acceleration of the argon jet is estimated to be $g \sim 10^{10}\,\mathrm{m/s}^2$ based on 3 or 4 snapshots taken by a fast-framing camera in visible band. A Rayleigh-Taylor instability is induced on the inner boundary of the kinked jet, with an axial wavelength $\lambda_z \sim 1 - 2\,\mathrm{cm}$ and an initial growth rate $\gamma \sim 10^6\,\mathrm{s}^{-1}$. See the left panel of Fig. 1 for a typical RT instability of a kinked argon jet. The RT instability quickly erodes and breaks the jet structure, leading to fast magnetic reconnection.[20,24] Hydrogen plasmas are found to develop kink instability in a very similar manner; but no distinct RT instability has been observed for hydrogen jets with $g \sim 10^{10}\,\mathrm{m/s}^2$; RT instabilities with axial wavelength $\lambda_z = 3 - 5\,\mathrm{cm}$ are observed only in some rare shots with strong lateral acceleration $g = 10^{11} - 3 \times 10^{11}\,\mathrm{m/s}^2$. We name the two cases as type I and type II hydrogen jets, respectively. The right two panels of Fig. 1 display the two types of hydrogen jets. The lateral acceleration in the experiment is possibly time-dependent, because it is caused by kink instability. However, due to the short life time of the RT instability and limitation of diagnostics, only one quantitative value of g is obtained.

These RT instabilities on one side of a magnetized cylindrical flux rope are interesting because they involve a complicated magnetic structure, a curved interface, and a lateral gravity that is not always perpendicular to the interface. In a naive attempt, we can assume locally the interface is a flat 2D plane. The bottom interface of the flux rope is susceptible to the interchange mode of RT instability, analogous to 2D magnetic RT theory. For argon plasma, the growth rate of such mode is $\gamma = \sqrt{2\pi g/\lambda_z} = 5 \times 10^6\,\mathrm{s}^{-1}$, which is very close to the observation. However, it is questionable that this interchange mode can exist at other parts of the interface. At the top, the gravity is pointing from vacuum to plasma and hence stabilizes the perturbation; at other locations the gravity is oblique to the interface. The oversimplified local 2D theory is therefore mathematically incompatible with the real case where lateral gravity is applied to a cylindrical interface. Moreover, it is also not clear why $\lambda_z = 1\,\mathrm{cm}$ is selected by the instability in argon plasma and why RT does not occur in type I hydrogen jets under the same lateral gravity.

Lateral RT instability in cylindrical geometry was previously considered in geophysics applications of diapir formation and spacing on a rising cylinder of buoyant hydrodynamic fluid.[25] References 26 and 27 show theoretically that the RT instability in cylindrical geometry differs significantly from the stability results for 1D or 2D planar interfaces, and that it is fundamentally incorrect to assume that results from planar geometry may be applied to cylindrical configurations.

It is therefore necessary to theoretically consider the lateral RT problem in a more rigorous way. In this paper, we

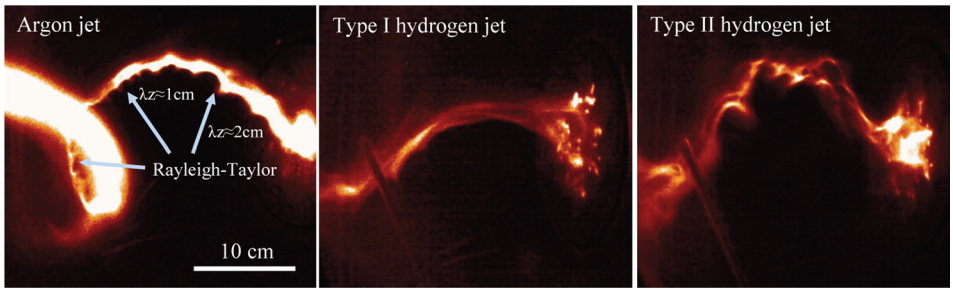

FIG. 1. Left: a kinked argon jet developing RT instability on the inner side of the surface with lateral acceleration $g \approx 4 \times 10^{10}\,\mathrm{m/s}^2$ (shot#13247, $t = 32\,\mu\mathrm{s}$). Middle: type I hydrogen jet with $g \approx 3 \times 10^{10}\,\mathrm{m/s}^2$ but no RT, (shot#11596, $t = 11\,\mu\mathrm{s}$). Right: type II hydrogen jet with $g \approx 1.5 \times 10^{11}\,\mathrm{m/s}^2$ having $\lambda_z \approx 4\,\mathrm{cm}$ RT instability (shot#11754, $t = 9.7\,\mu\mathrm{s}$). Images are taken by an IMACON 200 high speed camera in visible light. Magnetic field measurements show that actual radii of the jets (flux ropes) are 3–5 cm, larger than shown in the visible images.[19]

use linear stability analysis to develop an ideal MHD theory of Rayleigh-Taylor instability occurring on the surface of a magnetically collimated plasma-filled flux rope in vacuum with the presence of a gravity perpendicular to the plasma axis. We linearly perturb an equilibrium flux rope and decompose the perturbation into a summation over all azimuthal modes. It is found that the lateral gravity breaks the axisymmetry of the system, and consequentially couples all the azimuthal modes to each other. This mutual coupling of all the modes is converted to an eigenvalue problem where an eigenvector gives the amplitude of each azimuthal mode of an "eigen-perturbation" and the corresponding eigenvalue gives the growth rate of this eigen-perturbation. A parameter $\Phi^2 = gR/v_{A\theta}^2$ quantifies the relative importance of gravity versus azimuthal (toroidal) magnetic field, where R is the flux rope radius and $v_{A\theta} = B_\theta/\sqrt{\mu_0\rho}$ is the toroidal Alfvén speed on the plasma surface. In the weak gravity limit $\Phi^2 \ll 1$, different azimuthal modes are decoupled and the theory reduces to the classic current-driven instability ($m=-1$ kink instability). In the strong gravity limit $\Phi^2 \gg 1$, the theory reduces to the 1D hydrodynamic RT instability (Eq. (1)) or MRT instability (Eq. (2)). When both gravity and magnetic field are important, i.e., Φ^2 is of order of unity, the traditional Rayleigh-Taylor instability is coupled to the current-driven instability. This new hybrid instability, denoted as lateral Rayleigh-Taylor-current-driven (RT-CD) coupled instability, exhibits interesting features such as an intrinsic 3D geometry and quasi-paramagnetic properties that cannot be fully explained solely by either of the traditional instabilities. It is found that extremely small scale perturbations are suppressed and an optimal axial wavelength exists that gives the fastest growth rate. The theory successfully explains the Caltech experiments: in the argon plasma jet configuration, the theory predicts a coupled RT-CD instability with a $\lambda_z = 1.2\,\text{cm}$ and growth rate $\gamma = 3.6\times10^6\,\text{s}^{-1}$; for type I hydrogen jets, the theory shows only kink instability; for type II hydrogen jets, the theory shows some RT effect with a $\lambda_z \sim 5\,\text{cm}$.

This paper is arranged as follows. In Sec. II, we state the basic MHD equations and provide an equilibrium solution before perturbation. In Sec. III, we linearly perturb the equilibrium state and use the ideal MHD frozen-in flux condition to connect perturbations inside and outside the plasma. Section IV converts the partial differential equations to an eigenvalue problem of infinitely large matrices. In Sec. V, we solve the eigenvalue problem analytically and numerically and compare the results with existing theories and the lab experiments. Section VI summarizes the results and discusses other potential applications.

II. EQUATIONS AND EQUILIBRIUM STATE

In this paper we will primarily use cylindrical coordinates but will also use Cartesian coordinates from time to time. The two coordinate systems share a common z axis; the x and y axes of the Cartesian coordinates have respective azimuthal angles $\theta=0$ and $\pi/2$ in the cylindrical coordinates.

Consider an ideal MHD plasma in the presence of a lateral gravity field in the $-y$ direction. The MHD equations are

$$\frac{\partial\rho}{\partial t} + \nabla\cdot(\rho\mathbf{U}) = 0, \tag{3}$$

$$\rho\left(\frac{\partial\mathbf{U}}{\partial t} + \mathbf{U}\cdot\nabla\mathbf{U}\right) = \frac{1}{\mu_0}\mathbf{B}\cdot\nabla\mathbf{B} - \nabla\frac{B^2}{2\mu_0} - \nabla P - \rho g\hat{y}, \tag{4}$$

$$\frac{\partial\mathbf{B}}{\partial t} = \nabla\times(\mathbf{U}\times\mathbf{B}), \tag{5}$$

where all variables have their conventional meaning. Here, we assume the lateral gravity g is uniform and time-independent. In Eq. (4), the Lorentz force $\mathbf{J}\times\mathbf{B}$ has been split into a tension-like term and a pressure-like term.

As shown in Fig. 1, the scale of RT perturbations is much smaller than the major radius of the curved plasma tube. Therefore, we consider a straight, infinitely long cylindrical plasma tube along the z axis ($x=y=0$) which in equilibrium has radius R. Assume the plasma is incompressible and the plasma density is uniformly ρ_p inside the cylinder. To reduce complexity, we assume that axial current J_z is confined to the surface of the cylinder. Therefore, $B_{0\theta}=0$ inside the plasma. B_{0z} is continuous across the surface, hence $J_{0\theta}=0$. Here, the subscript 0 refers to equilibrium quantities. Outside the plasma is vacuum. Therefore, the density profile in equilibrium is $\rho_0 = \rho_p\cdot H(R-r)$, where $H(x)$ is the Heaviside step function: $H(x)=0$ for $x<0$ and $H(x)=1$ for $x>0$.

In the experiment, the plasma jet continues to elongate and the kink instability keeps growing. For an argon jet experiment, the jet flow rate can be calculated by $\gamma_{flow} \sim v_{jet}/L \sim 10^4\,\text{s}^{-1}$ where $v_{jet}\sim 10\,\text{km/s}$ and $L\sim 30\,\text{cm}$. The kink instability grows at a rate of $\gamma_{kink}\sim 10^5\,\text{s}^{-1}$ (see Ref. 20). Both jet flow and kink thus occur at much lower rates compared to the RT instability. Therefore, we ignore the flow effect and kink dynamics within the microseconds duration of RT instability and assume a static pre-RT equilibrium with the presence of an effective gravity.

Without gravity, the equilibrium is simply a classic Z-pinch, which has a uniform pressure $P_0 = B_{0\theta}(R+)^2/(2\mu_0)$ inside plasma, where $B_{0\theta}(R+)$ is the toroidal field just outside the plasma tube.[2] However, with the gravity, a mechanism that can support the plasma tube against the gravity is required. The y component of Lorentz force in Cartesian coordinates is

$$(\mathbf{J}\times\mathbf{B})_y = J_zB_x - J_xB_z. \tag{6}$$

In Appendix A, we show that the first term J_zB_x corresponds to the hoop force of an arched flux rope, where the effective B_x is a natural consequence of the kinked plasma tube bending as a half torus flux rope. The second term J_xB_z corresponds to a magnetic buoyancy effect, which requires a y-dependent axial field $B_z(y)$ that gives a horizontal current density J_x. Detailed quantitative analyses in Appendix A also show that the magnetic field in equilibrium is nearly azimuthally symmetric, i.e., the B_x component in the hoop force scenario and the y-dependent component of B_z are both

negligible compared to $B_{0\theta}$ at $r = R+$ and B_{0z} along the z axis. We therefore make an approximation and assume that the equilibrium magnetic field of the system is

$$\mathbf{B}_0 = b_z\hat{z} + b_\theta \frac{R}{r} H(r-R)\hat{\theta}, \tag{7}$$

where $\mathbf{B}_{0z} = b_z\hat{z}$ is uniform both inside and outside the plasma tube, and $\mathbf{B}_{0\theta} = b_\theta \frac{R}{r} H(r-R)\hat{\theta}$ is azimuthally symmetric and only exists outside the plasma tube. Without loss of generality, we assume $b_z > 0$ and $b_\theta > 0$, which gives a right-hand helical magnetic field.

The assumption of a surface current J_z is a common practice in analytical derivations, because this assumption greatly reduces mathematical complicity while capturing the key underlying physics (e.g., see Ref. 4). In the experiment, at $T \sim 5\,\text{eV}$ the Spitzer resistivity is $\eta \sim 10^{-4}\,\Omega\,\text{m}$. With RT growth rate $\gamma \sim 10^6\,\text{s}^{-1}$, plasma skin depth $\delta \sim (\eta/(2\pi\gamma\mu_0))^{1/2} \sim 1\,\text{mm}$ is much less than the plasma jet radius. A current can theoretically exist with similar thickness near the plasma tube boundary, and hence can be regarded as a surface current. In a more realistic configuration where axial current density J_z is finite inside the plasma, a shear of the magnetic field exists in the radial direction because $B_{0\theta}(r) = \mu I(r)/(2\pi r)$ depends on r as does the pitch angle $\alpha = B_{0z}/B_{0\theta}$. This shear is stabilizing because a paramagnetic perturbation on plasma surface will not be aligned with magnetic field inside the plasma.[2] Therefore, the surface-current-based equilibrium also gives the most unstable instability.

III. PERTURBATION AND LINEARIZATION

We now perturb the equilibrium state and use the subscript "1" to indicate the first order perturbed quantities. Consider a random initial perturbations with axial wavenumber k

$$g_k(r,\theta,z,t) = e^{ikz}\left[\sum_q e^{\gamma_{k,q}t} h_q(r,\theta)\right], \tag{8}$$

i.e., the perturbation may contain multiple modes growing at different rate $\gamma_{k,q}$ and each mode involves both r and θ. Expand $h_q(r,\theta)$ as a summation of all normal modes $\sum_m f_m(r)e^{im\theta}$. For each fixed k, the goal is to find the most unstable mode q with the largest real part of $\gamma_{k,q}$, denoted as $\gamma_k = \max_n \gamma_{k,q}$. Then find k which maximizes the real part of γ_k. In the following derivation, we will omit the summation symbols by writing all the perturbed quantities in the form of $f(r)e^{\gamma t + im\theta + ikz}$, where γ is a complex number and m is integer. Without loss of generality, we assume $k > 0$.

The perturbed continuity equation reads

$$\gamma\delta\rho + \rho_0\nabla\cdot\delta\mathbf{U} + \delta\mathbf{U}\cdot\nabla\rho_0 = 0,$$

where δ^* is the difference between any quantity $*$ and its unperturbed value. The second term corresponds to the plasma compressibility. There is $|\rho_0\nabla\cdot\delta\mathbf{U}/(\gamma\delta\rho)| \sim |\rho_0\delta U_r/(\gamma R\delta\rho)| \sim 0.1 \ll 1$. Here, $\gamma \sim 3\times10^6\,\text{s}^{-1}$, $R = 3\text{cm}$, $\delta\rho \sim \rho_0$ based on recent Stark broadening spectroscopic measurement,[24] and $\delta U_r \sim 10\text{km/s}$ estimated from Fig. 3 of Ref. 20. This simple semi-quantitative analysis shows that the perturbation can be considered to be incompressible

$$\nabla\cdot\mathbf{U}_1 = 0. \tag{9}$$

This is consistent with the MHD energy principle[2,28] which shows that the most unstable mode is incompressible. The linearized versions of Eqs. (3)–(5) are

$$\rho_1 = -\frac{1}{\gamma}\mathbf{U}_1\cdot\nabla\rho_0 = -\frac{1}{\gamma}U_{1r}\frac{\partial\rho_0}{\partial r}, \tag{10}$$

$$\gamma\frac{\rho_0}{\rho_p}\mathbf{U}_1 = -\nabla\left(\frac{P_1}{\rho_p} + \frac{b_\theta^2}{\rho_p}\frac{\bar{\mathbf{B}}_0\cdot\bar{\mathbf{B}}_1}{\mu_0}\right) + \frac{b_\theta^2}{\rho_p}\frac{\bar{\mathbf{B}}_0\cdot\nabla\bar{\mathbf{B}}_1}{\mu_0} + \frac{b_\theta^2}{\rho_p}\frac{\bar{\mathbf{B}}_1\cdot\nabla\bar{\mathbf{B}}_0}{\mu_0} + \frac{g}{\gamma\rho_p}U_{1r}\frac{\partial\rho_0}{\partial r}\hat{y}, \tag{11}$$

$$\gamma\bar{\mathbf{B}}_1 = \nabla\times(\mathbf{U}_1\times\bar{\mathbf{B}}_0), \tag{12}$$

where the magnetic field terms are all normalized to $b_\theta = B_{0\theta}(R+)$, i.e., $\bar{\mathbf{B}}_0 = \mathbf{B}_0/b_\theta$ and $\bar{\mathbf{B}}_1 = \mathbf{B}_1/b_\theta$. The continuity Eq. (10) has been used to eliminate ρ_1 in the momentum Eq. (11). Both sides of Eq. (11) have been multiplied by the constant $1/\rho_p$.

We define the toroidal Alfvén speed $v_{A\theta} = b_\theta/\sqrt{\mu_0\rho_p}$ and dimensionless parameters

$$\Phi^2 = \frac{gR}{v_{A\theta}^2} \quad \alpha = \frac{b_z}{b_\theta} \quad \Gamma = \frac{\gamma^2R^2}{v_{A\theta}^2} \quad x = kR \quad q = \alpha x. \tag{13}$$

The Alfvén speed $v_{A\theta}$, the parameter Φ^2 and α are all determined by the equilibrium state. α is the pitch angle of the helical magnetic field on the interface. Γ is the dimensionless growth rate; $q = \alpha x = kRb_z/b_\theta$ is the safety factor of the perturbation with $x = kR$.

We divide Eq. (11) by $v_{A\theta}^2$ to obtain

$$\frac{\gamma}{v_{A\theta}^2}\frac{\rho_0}{\rho_p}\mathbf{U}_1 = -\nabla\bar{P}_1 + \bar{\mathbf{B}}_0\cdot\nabla\bar{\mathbf{B}}_1 + \bar{\mathbf{B}}_1\cdot\nabla\bar{\mathbf{B}}_0 + \frac{\Phi^2}{\gamma\rho_pR}U_{1r}\frac{\partial\rho_0}{\partial r}\hat{y}, \tag{14}$$

where we have defined the effective pressure perturbation

$$\bar{P}_1 = \frac{P_1}{\rho_p v_{A\theta}^2} + \bar{\mathbf{B}}_0\cdot\bar{\mathbf{B}}_1. \tag{15}$$

The radial and axial components of Eq. (14) are

$$\frac{\gamma}{v_{A\theta}^2}\frac{\rho_0}{\rho_p}U_{1r} = -\frac{\partial\bar{P}_1}{\partial r} + (\bar{\mathbf{B}}_0\cdot\nabla\bar{\mathbf{B}}_1 + \bar{\mathbf{B}}_1\cdot\nabla\bar{\mathbf{B}}_0)_r + \frac{\Phi^2}{\gamma\rho_pR}U_{1r}\frac{\partial\rho_0}{\partial r}\sin\theta, \tag{16}$$

$$\frac{\gamma}{v_{A\theta}^2}\frac{\rho_0}{\rho_p}U_{1z} = -\frac{\partial\bar{P}_1}{\partial z} + (\bar{\mathbf{B}}_0\cdot\nabla\bar{\mathbf{B}}_1 + \bar{\mathbf{B}}_1\cdot\nabla\bar{\mathbf{B}}_0)_z. \tag{17}$$

To compute $\bar{\mathbf{B}}_1$, Eq. (12) is dotted with ∇h where h is an arbitrary analytic function. This gives

$$\begin{aligned}\gamma\nabla h\cdot\bar{\mathbf{B}}_1 &= \nabla h\cdot\nabla\times(\mathbf{U}_1\times\bar{\mathbf{B}}_0),\\ &= \nabla\cdot((\mathbf{U}_1\times\bar{\mathbf{B}}_0)\times\nabla h)+(\mathbf{U}_1\times\bar{\mathbf{B}}_0)\cdot\nabla\times\nabla h,\\ &= \nabla\cdot(\bar{\mathbf{B}}_0\mathbf{U}_1\cdot\nabla h-\mathbf{U}_1\bar{\mathbf{B}}_0\cdot\nabla h),\\ &= \bar{\mathbf{B}}_0\cdot\nabla(\mathbf{U}_1\cdot\nabla h)-\mathbf{U}_1\cdot\nabla(\bar{\mathbf{B}}_0\cdot\nabla h).\end{aligned}\tag{18}$$

Taking $h=r$, $h=\theta$, and $h=z$ in the equation, respectively, and noting that $\bar{\mathbf{B}}_0\cdot\hat{r}=0$ and $\bar{\mathbf{B}}_0\cdot\hat{z}=\bar{B}_{0z}$ are constant, we obtain

$$\bar{B}_{1r}=\frac{1}{\gamma}\bar{\mathbf{B}}_0\cdot\nabla U_{1r},\tag{19}$$

$$\bar{B}_{1\theta}=\frac{r}{\gamma}\left[\bar{\mathbf{B}}_0\cdot\nabla\left(\frac{U_{1\theta}}{r}\right)-\mathbf{U}_1\cdot\nabla\left(\frac{\bar{B}_{0\theta}}{r}\right)\right],\tag{20}$$

$$\bar{B}_{1z}=\frac{1}{\gamma}\bar{\mathbf{B}}_0\cdot\nabla U_{1z}.\tag{21}$$

The magnetic field perturbation is therefore expressed in terms of the equilibrium magnetic field subject to small motion of plasma, as a direct result of the ideal MHD frozen-in flux condition.

A. Magnetic field perturbation

In the equilibrium state, $\mathbf{J}_0=J_{0z}\hat{z}$ is non-zero only on the plasma surface. It can be proved that the perturbed current $\mathbf{J}_1$ is also confined on the surface (See the Appendix B). Therefore, $\nabla\times\mathbf{B}_1=0$ both inside and outside the plasma. This means that there exists a scalar "potential" χ where $\bar{\mathbf{B}}_1=\nabla\chi$ and

$$\nabla^2\chi=\nabla\cdot\bar{\mathbf{B}}_1=0.\tag{22}$$

Here, χ is a linear perturbation term and has the form of $\chi\sim\sum f_m(r)e^{\gamma t+im\theta+ikz}$. Solving the equation in cylindrical coordinates and requiring regularity at $r=0$ and $+\infty$ gives

$$\chi=\begin{cases}\sum_m a_m I_m(kr)e^{\gamma t+im\theta+ikz} & r<R\\ \sum_m b_m K_m(kr)e^{\gamma t+im\theta+ikz} & r>R,\end{cases}\tag{23}$$

where the summations are over all integers m, $I_m(x)$ and $K_m(x)$ are the modified Bessel functions of the first kind and the second kind, respectively. In the following content, we will use I_m, K_m, I'_m and K'_m to represent the corresponding functions or their first order derivative evaluated at $x=kR$.[29]

Coefficients a_m and b_m are related by the fact that the perturbed magnetic field cannot penetrate the surface of plasma according to the ideal MHD frozen-in flux condition. This is satisfied by the MHD induction equation (Eqs. (19)–(21)) plus continuity at the plasma interface. The latter condition requires that the velocity component orthogonal to the interface must be continuous across the interface, i.e.,

$$U_{1r}(R-)=U_{1r}(R+).\tag{24}$$

Since $\bar{B}_0=\alpha\hat{z}$ inside plasma and $\bar{B}_0=\alpha\hat{z}+(R/r)\hat{\theta}$ outside plasma, Eq. (19) can be written explicitly as

$$\bar{B}_{1r}=\begin{cases}ik\alpha U_{1r}/\gamma & r<R\\ (imR/r^2+ik\alpha)U_{1r}/\gamma & r>R,\end{cases}\tag{25}$$

for each m mode, where we have used $\hat{z}\cdot\nabla=\partial_z=ik$ and $\hat{\theta}\cdot\nabla=(1/r)\partial_\theta=im/r$. Equation (23) gives $\bar{B}_{1r}(R-)=a_mkI'_m$ and $\bar{B}_{1r}(R+)=b_mkK'_m$. Hence

$$a_mkI'_m=ik\alpha U_{1r}(R-)/\gamma,\tag{26}$$

$$b_mkK'_m=\left(\frac{im}{R}+ik\alpha\right)U_{1r}(R+)/\gamma.\tag{27}$$

Applying Eq. (24) to Eqs. (26) and (27) gives

$$b_m=\frac{m+q}{q}\frac{I'_m}{K'_m}a_m.\tag{28}$$

The vacuum field is now expressed in terms of the plasma field.

Inside the plasma, $\bar{\mathbf{B}}_0=\alpha\hat{z}$ is uniform so Eqs. (19)–(21) reduce to $\mathbf{B}_1=(1/\gamma)\bar{\mathbf{B}}_0\cdot\nabla\mathbf{U}_1=(ik\alpha/\gamma)\mathbf{U}_1$ and

$$\mathbf{U}_1=\frac{\gamma}{ik\alpha}\bar{\mathbf{B}}_1.\tag{29}$$

Equation (17) and the z component of Eq. (29) give

$$\bar{P}_1(R-)=\left(\alpha+\frac{\gamma^2}{\alpha k^2v_{A\theta}^2}\right)\bar{B}_{1z}(R-)=ik\alpha\left(1+\frac{\Gamma}{q^2}\right)a_mI_m,\tag{30}$$

where Γ and q are defined in Eq. (13).

Outside the plasma, $\bar{\mathbf{B}}_0(R+)=\alpha\hat{z}+\hat{\theta}$. Hence

$$\begin{aligned}\bar{P}_1(R+) &= \bar{\mathbf{B}}_0(R+)\cdot\bar{\mathbf{B}}_1(R+)=\bar{B}_{1\theta}(R+)+\alpha\bar{B}_{1z}(R+)\\ &= \frac{im}{R}b_mK_m+ik\alpha b_mK_m\\ &= \frac{i}{R}\frac{(m+q)^2}{q}\frac{I'_mK_m}{K'_mI_m}a_mI_m,\end{aligned}\tag{31}$$

where Eq. (28) has been used.

IV. RADIAL MOTION JUMP CONDITION AT THE INTERFACE

The interface region where the current flows is part of the plasma and so is governed by the MHD equations, i.e., the momentum equation and the induction equation.

We integrate the radial motion Eq. (16) across the interface from $r=R-$ to $R+$ to obtain

$$\begin{aligned}0 = -\bar{P}_1|_{R_-}^{R_+}+\int_{R_-}^{R_+}(\bar{\mathbf{B}}_0\cdot\nabla\bar{\mathbf{B}}_1+\bar{\mathbf{B}}_1\cdot\nabla\bar{\mathbf{B}}_0)_r dr\\ -\frac{\Phi^2}{\gamma R}U_{1r}(R-)\sin\theta.\end{aligned}\tag{32}$$

For general cylindrical vectors

$$(\mathbf{F}\cdot\nabla\mathbf{G})_r=F_r\frac{\partial G_r}{\partial r}+\frac{F_\theta}{r}\frac{\partial G_r}{\partial\theta}+F_z\frac{\partial G_r}{\partial z}-\frac{F_\theta G_\theta}{r},\tag{33}$$

and also because $\bar{B}_{0r}=0$ and $\bar{B}_{0z}=\alpha$

$$(\bar{\mathbf{B}}_0\cdot\nabla\bar{\mathbf{B}}_1+\bar{\mathbf{B}}_1\cdot\nabla\bar{\mathbf{B}}_0)_r=\frac{im}{r}\bar{B}_{0\theta}\bar{B}_{1r}+ik\alpha\bar{B}_{1r}-\frac{2\bar{B}_{0\theta}\bar{B}_{1\theta}}{r}. \tag{34}$$

The second term of Eq. (32) involves an integration across an infinitesimally thin layer. Only terms behaving like a delta-function at $r=R$ contribute to this integration. These terms must contain a partial derivative at $r=R$ in the radial direction. On examination of Eqs. (19)–(21), it is seen that only $\bar{B}_{1\theta}$ is a delta-function type term. To see this, rewrite Eq. (20) and only keep the term with ∂_r to obtain

$$\bar{B}_{1\theta}=-\frac{r}{\gamma}U_{1r}\frac{\partial}{\partial r}\left(\frac{\bar{B}_{0\theta}}{r}\right)+\text{non-delta}. \tag{35}$$

Therefore,

$$\begin{aligned}(\bar{\mathbf{B}}_0\cdot\nabla\bar{\mathbf{B}}_1+\bar{\mathbf{B}}_1\cdot\nabla\bar{\mathbf{B}}_0)_r&=\frac{2}{\gamma}U_{1r}\bar{B}_{0\theta}\frac{\partial}{\partial r}\left(\frac{\bar{B}_{0\theta}}{r}\right)+\text{non-delta}\\&=\frac{U_{1r}}{\gamma r}\frac{\partial\bar{B}_{0\theta}^2}{\partial r}+\text{non-delta}.\end{aligned} \tag{36}$$

Integration across the interface gives

$$\begin{aligned}&\int_{R-}^{R+}(\bar{\mathbf{B}}_0\cdot\nabla\bar{\mathbf{B}}_1+\bar{\mathbf{B}}_1\cdot\nabla\bar{\mathbf{B}}_0)_r dr\\&=\frac{U_{1r}(R+)}{\gamma R}\bar{B}_{0\theta}(R+)^2\\&=\frac{U_{1r}(R+)}{\gamma R}=\frac{U_{1r}(R-)}{\gamma R}=\frac{k}{iq}a_m I'_m,\end{aligned} \tag{37}$$

where Eqs. (24) and (26) have been used.

The last term in Eq. (32) is given by the lateral gravity. We write $\sin\theta=(e^{i\theta}-e^{-i\theta})/2i$ and expand U_{1r} using Eq. (26) to obtain

$$\begin{aligned}&\frac{\Phi^2}{\gamma R}U_{1r}(R-)\sin\theta\\&=\frac{\Phi^2}{i\alpha kR}\frac{e^{i\theta}-e^{-i\theta}}{2i}\sum_m a_m k I'_m e^{im\theta}\\&=-\frac{\Phi^2 k}{2q}\sum_m a_m I'_m\left(e^{i(m+1)\theta}-e^{i(m-1)\theta}\right)\\&\overset{m^{th}}{=}-\frac{\Phi^2 k}{2q}\left(a_{m-1}I'_{m-1}-a_{m+1}I'_{m+1}\right).\end{aligned} \tag{38}$$

This shows that the lateral gravity breaks the axisymmetry of the cylindrical system and links the mth mode to the $(m\pm1)$th modes.

Substitution of Eqs. (30), (31), (37), and (38) into Eq. (32) gives

$$\begin{aligned}0=&ik\alpha\left(1+\frac{\Gamma}{q^2}\right)a_m I_m-\frac{i}{R}\frac{(m+q)^2}{q}\frac{I'_m K_m}{K'_m I_m}a_m K_m\\&+\frac{k}{iq}a_m I'_m+\frac{\Phi^2 k}{2q}\left(a_{m-1}I'_{m-1}-a_{m+1}I'_{m+1}\right).\end{aligned} \tag{39}$$

We multiply by iRq to obtain

$$\begin{aligned}&(m+q)^2\frac{I'_m K_m}{K'_m I_m}a_m K_m+xa_m I'_m+\frac{i}{2}x\Phi^2\\&\times\left(a_{m-1}I'_{m-1}-a_{m+1}I'_{m+1}\right)=\left(\Gamma+q^2\right)a_m I_m.\end{aligned} \tag{40}$$

The above equation is a very strong condition because it holds for all integers m. This shows that a normal mode $f(r)e^{im\theta+ikz}$ is in general not an eigen perturbation, or equivalently an eigen perturbation to the system is a combination of all normal modes. Equation (40) is not to be considered as a coefficient recurrence relation, because one should not expect an arbitrary perturbation to precisely satisfy the condition for all azimuthal modes. Instead, Eq. (40) should be considered as an eigenvalue problem. We define new coefficients

$$w_m\equiv a_m I_m\quad\text{for all integer}\,m, \tag{41}$$

an infinitely long column vector

$$\mathbf{w}\equiv[\cdots,w_{-2},w_{-1},w_0,w_1,w_2,\ldots]^T, \tag{42}$$

an infinitely large zero-diagonal-entry tridiagonal matrix

$$\mathbf{G}=(G_{mn})_{m,n\in\mathbf{Z}}\quad G_{m+1,m}=-G_{m-1,m}=x\frac{I'_m}{I_m}, \tag{43}$$

two infinitely large diagonal matrices

$$\mathbf{M}=(M_{mn})_{m,n\in\mathbf{Z}}\quad M_{m,m}=(m+q)^2\frac{I'_m}{I_m}\frac{K_m}{K'_m}, \tag{44}$$

$$\mathbf{N}=(N_{mn})_{m,n\in\mathbf{Z}}\quad N_{m,m}=x\frac{I'_m}{I_m}, \tag{45}$$

and an infinitely large tridiagonal matrix

$$\mathbf{Q}\equiv\mathbf{M}+\mathbf{N}+\frac{i}{2}\Phi^2\mathbf{G}. \tag{46}$$

Equation (40) becomes

$$\begin{aligned}\left[\mathbf{M}+\mathbf{N}+\frac{i}{2}\Phi^2\mathbf{G}\right]\mathbf{w}&=\left(\Gamma+q^2\right)\mathbf{w},\\\mathbf{Q}\mathbf{w}&=(\Gamma+q^2)\mathbf{w}.\end{aligned} \tag{47}$$

The infinite matrix $\mathbf{Q}$ has an infinite and countable number of eigenvalues $\{\sigma^m\}_{m\in\mathbf{Z}}$ and eigenvectors $\{\mathbf{w}^m\}_{m\in\mathbf{Z}}$. Each eigenvector gives the coefficients $\{a_m\}$ of an eigen-perturbation. The growth rate of this eigen-perturbation is given by the corresponding eigenvalue. All of the eigen-perturbations form a complete basis and any arbitrary perturbation can always be decomposed into a linear combination of those eigen-perturbations, and the fastest growing mode is the eigen-perturbation with the largest positive Γ. A similar treatment but for the situations of diapir formation can be found in Refs. 26 and 27. Note that because of the lateral gravity and the cylindrical geometry, an eigen-perturbation contains all azimuthal modes because the matrix $\mathbf{Q}$ is non-diagonal.

A. Preliminary analysis on stability

We multiply Eq. (40) by $(v_{A\theta}^2/R^2)/(a_m I_m)$ to obtain

$$\frac{v_{A\theta}^2}{R^2}(m+q)^2\frac{I'_m K_m}{I_m K'_m}+\frac{v_{A\theta}^2}{R}k\frac{I'_m}{I_m}+\frac{i}{2}gk \times\frac{a_{m-1}I'_{m-1}-a_{m+1}I'_{m+1}}{a_m I_m}=\gamma^2+\alpha^2k^2v_{A\theta}^2. \quad (48)$$

This pre-matrix equation has a one-to-one correspondence with Eq. (47) and provides more physical intuition.

For $x>0$ $I_m>0$, $K_m>0$, $I'_m>0$, and $K'_m<0$, so $M_{mm}<0$, $N_{mm}>0$, $G_{m+1,m}>0$, and $G_{m-1,m}<0$.

All diagonal entries of the diagonal matrix $\mathbf{M}$ are negative. Larger $|M_{mm}|$ results in smaller Γ and so a more stable system. The dimensioned version of $\mathbf{M}$ is given by the first term of Eq. (48), hence

$$\mathbf{M}_{mm}\propto\frac{b_\theta^2}{R^2}(m+q)^2=\left(\frac{m}{R}b_\theta+kb_z\right)^2=(\mathbf{k}\cdot\mathbf{B})^2, \quad (49)$$

where $\mathbf{k}=k\hat{z}+(m/R)\hat{\theta}$ and $\mathbf{B}=b_z\hat{z}+b_\theta\hat{\theta}$ are the instability wavevector and magnetic field on the plasma surface, respectively. Therefore, $\mathbf{M}$ represents the stabilizing effect due to the tension along the magnetic field.

$\mathbf{N}$ is a positive-definite matrix and hence destabilizes the system. The second term of Eq. (48) shows that $\mathbf{N}$ is proportional to $v_{A\theta}^2/R$, which can be understood as the centrifugal acceleration a test particle experiences when traveling around the $r=R$ interface at the Alfvén speed $v_{A\theta}$. Therefore, the destabilizing effect is a result of "bad" curvature of the azimuthal magnetic field on the circular plasma-vacuum interface. The destabilizing effect leads to a traditional current-driven instability.

The gravity term $i\mathbf{G}$ does not have a simple stabilizing or destabilizing effect. Since $\mathbf{G}$ is similar to a skew-symmetric matrix and $i\mathbf{G}$ is similar to a Hermitian matrix, all the eigenvalues of $i\mathbf{G}$ are pure real and they are in positive-negative pairs, i.e., if $\lambda>0$ is an eigenvalue then $-\lambda$ is also an eigenvalue. Positive eigenvalues correspond to a destabilizing effect, and negative ones stabilize the system. This can be understood intuitively by considering a perturbation occurring around the cylindrical plasma: the perturbation on the "top" of the surface (i.e., $y>0$) undergoes a stable oscillation, and a perturbation on the "bottom" of the surface ($y<0$) undergoes a RT instability. Another important feature of $i\mathbf{G}$ is that it is the only non-diagonal matrix in Eq. (47). The first sub-diagonal and super-diagonal entries of $i\mathbf{G}$ are nonzero. Therefore, any azimuthal mode m is coupled with neighboring modes $m-1$ and $m+1$ due to $i\mathbf{G}$, and hence all azimuthal modes are coupled.

The second term of the RHS of Eq. (48), $\alpha^2k^2v_{A\theta}^2$, is proportional to $k^2b_z^2$ and hence corresponds to tension along the axial magnetic field. This term helps to reduce γ^2 for fixed Γ and therefore stabilizes the system.

As a short summary, B_z and B_θ help stabilize the system because of magnetic tension; however, the "bad" curvature of B_θ destabilizes the system; the gravity term has a dual effect which stabilizes some perturbations and destabilizes others; the gravity term also breaks the azimuthal symmetry and couples all azimuthal modes.

B. Comments on the matrix equation

Equation (47) involves infinitely large matrices that cannot be solved directly. However, in practice, approximate solutions can be obtained by truncating the matrices. We define a series of finite matrices

$$\mathbf{Q}_p\equiv(Q_{mn})_{-p\le m,n\le p},\quad p=1,2,3,\ldots \quad (50)$$

For each integer p, $\mathbf{Q}_p$ is a $(2p+1)$ by $(2p+1)$ square tridiagonal matrix. We solve the eigenvalue problems $\mathbf{Q}_p\mathbf{w}_p^q=\sigma_p^q\mathbf{w}_p^q$ in a complex space, where $q\in\{1,2,\ldots,2p+1\}$ is the index of the eigenvalues and eigenvectors of $\mathbf{Q}_p$. We sort the eigenvalues in descending order by their real parts, i.e., $\mathrm{real}(\sigma_p^1)\ge\cdots\ge\mathrm{real}(\sigma_p^{2p+1})$. We solve the above systems with successively increasing p and look for limits

$$\lim_{p\to+\infty}\sigma_p^1\to\sigma^1,\quad \lim_{p\to+\infty}\mathbf{w}_p^1\to\mathbf{w}^1. \quad (51)$$

We numerically verify that the above limits always exist because $\mathbf{M}$ has a very strong stabilizing effect to large $|m|$. σ^1 gives the growth rate of the fastest growing mode by $\Gamma=\sigma^1-q^2$, while $\mathbf{w}^1$ gives the coefficients of each azimuthal mode of the fastest growing mode. If there exist some mechanism inhibiting high-order azimuthal modes, p can be chosen to be the highest permitted azimuthal mode number. In this paper, we choose $p=70$.

In the derivation we have assumed that g is constant because the experiment cannot resolve the time-dependent profile of g. Equation (47), although derived assuming constant g, in fact remains valid at any time snapshot if g is time-dependent. However the growth rate Γ and eigenvectors $\mathbf{w}$ are now also time-dependent because Φ^2 changes with time.

V. SOLUTIONS

We now solve Eq. (47). We first consider several special cases where either gravity or the magnetic field is weak. In these cases, some analytical solutions can be obtained using short or long wavelength approximations. Then we numerically solve the truncated matrix equation for general cases.

A. Weak gravity or strong toroidal magnetic field limit

The limit of weak gravity or strong toroidal magnetic field is defined by $\Phi^2=gR/v_{A\theta}^2\ll1$, or equivalently $g\ll v_{A\theta}^2/R$. In this limit, Eq. (47) becomes

$$(\mathbf{M}+\mathbf{N})\mathbf{w}=(\Gamma+q^2)\mathbf{w}. \quad (52)$$

Since both $\mathbf{M}$ and $\mathbf{N}$ are diagonal matrices, each $e^{im\theta}$ mode is now an eigen mode of the system because there is no gravity breaking the axisymmetry. The growth rate of the mth mode simply is

$$\Gamma=M_{mm}+N_{mm}-q^2, \quad (53)$$

$$\gamma^2 = \frac{v_{A\theta}^2}{R^2}\left((m+q)^2\frac{I'_m K_m}{I_m K'_m} + x\frac{I'_m}{I_m} - q^2\right). \tag{54}$$

The marginal stability is given by

$$(m+q)^2\frac{I'_m K_m}{I_m K'_m} + x\frac{I'_m}{I_m} - q^2 < 0. \tag{55}$$

At this point, we have returned to the textbook current-driven MHD instability. Equation (10.171) in Ref. 2 shows that for such system in no-walled vacuum, the marginal stability is given by

$$kR\frac{b_z^2}{b_\theta^2}\frac{I_m}{I'_m} - \frac{(m+q)^2}{kR}\frac{K_m}{K'_m} > 1. \tag{56}$$

After multiplying by $x(I'_m/I_m)$ on both sides the inequality becomes identical to Eq. (55). Therefore, the theory reduces to classic current-driven MHD instability in the weak gravity limit. In the long wavelength approximation $k^2R^2 \ll m$, the modified Bessel functions give $I'_m/I_m \approx |m|/x$ and $K'_m/K_m \approx -|m|/x$ (Ref. 29). Equation (54) becomes

$$\gamma^2 = \frac{v_{A\theta}^2}{R^2}\left(-(m+q)^2 + |m| - q^2\right), \tag{57}$$

which is positive for $m=-1$ when $q<1$. This is the classic $m=-1$ kink instability.

B. Strong gravity or weak toroidal magnetic field limit

In the limit of $\Phi^2 \gg 1$ or equivalently $g \gg v_{A\theta}^2/R$, Eq. (47) becomes

$$\frac{i}{2}\Phi^2\mathbf{G}\mathbf{w} = \left(\Gamma + q^2\right)\mathbf{w}. \tag{58}$$

Consider the short wavelength approximation $kR \gg p^2$ with the matrix $\mathbf{G}$ intentionally truncated at $\pm p$. In this limit $I'_m/I_m \approx 1$ for $|m| \le p$ (Ref. 29). Hence, all the sub-diagonal entries of $\mathbf{G}_p$ are x and all the super-diagonal entries are $-x$. $i\mathbf{G}_p$ is then a Toeplitz matrix and the eigenvalues are $2x\cos(k\pi/(2p+2))$, where $k = 1, \ldots, 2p+1$ (Ref. 30). The largest eigenvalue of $i\mathbf{G}$ is $2x$. So

$$\Gamma = x\Phi^2 - q^2 = x\Phi^2 - \alpha^2x^2, \tag{59}$$

$$\gamma^2 = gk - \frac{b_z^2k^2}{\mu_0\rho_0} = gk - v_{Az}^2k^2, \tag{60}$$

where $v_{Az} = b_z/\sqrt{\mu_0\rho_p} = \alpha v_{A\theta}$. This is the 1D MRT theory for the undular mode along the axial direction. In the zero field limit $b_z = 0$, the short wavelength approximation gives $\gamma^2 = gk$, which is the 1D hydrodynamic RT instability. The short wavelength approximation emphasizes axial perturbation and ignores azimuthal perturbation. This explains why under short wavelength approximation the theory is identical to 1D MRT.

The maximum of Γ or γ^2 occurs for x that satisfies $d\Gamma/dx = 0$. From Eq. (60) this maximum is obtained at

$$\begin{aligned} x &= \Phi^2/(2\alpha^2) & \max\Gamma &= \Phi^4/(4\alpha^2), \\ k &= g/(2v_{Az}^2) & \max\gamma &= g/(2v_{Az}). \end{aligned} \tag{61}$$

It is notable that Eq. (58) is an ill-posed problem unless $\mathbf{G}$ is truncated. Otherwise there are always sufficiently large integers p so that the short wavelength approximation fails. The extreme case is when the long wavelength approximation is valid, i.e., $kR \ll \sqrt{p}$, $G_{p+1,p} = xI'_p/I_p \approx |p|$. Therefore, the non-zero elements of $\mathbf{G}$ diverge as $p \to +\infty$, and so do the eigenvalues.

C. Lateral Rayleigh-Taylor-current-driven coupled instability in cylindrical MHD collimated plasma

We have shown that the solution reduces to the conventional current-driven MHD instability and the 1D hydrodynamic/magnetic Rayleigh-Taylor instability when either gravity or (toroidal) magnetic field is neglected. When both gravity and magnetic field are present, the two instabilities are expected to couple together and give a RT-CD coupled instability.

In the Caltech plasma jet experiment, a typical argon jet has $n_e = n_i = 10^{22}\,\mathrm{m}^{-3}$, $I_z = 60\,\mathrm{kA}$, $R = 3.5\,\mathrm{cm}$, $B_z = 0.2\,\mathrm{T}$ so $B_\theta = 0.34\,\mathrm{T}$. Hence $\alpha = 0.583$. A typical effective gravity is $g = 4\times10^{10}\,\mathrm{m/s}^2$ (See Ref. 20) hence $\sqrt{gR} = 34.6\,\mathrm{km/s}$. Other system parameters are $v_{Az} = 6.9\,\mathrm{km/s}$, $v_{A\theta} = 11.8\,\mathrm{km/s}$ and $\Phi^2 = 10$. For type I hydrogen jet with the same g and R, the parameters are $v_{Az} = 43.6\,\mathrm{km/s}$, $v_{A\theta} = 74.8\,\mathrm{km/s}$ and $\Phi^2 = 0.25$. It is seen that due to the different ion weight, the gravity effect is important in the argon jet while the current-driven effect dominates in type I hydrogen jet.

Despite the complexity of the theory, Eq. (47) has only three free parameters. Given x, Φ^2 and α (or kR, $gR/v_{A\theta}^2$ and b_z/b_θ), the three matrices $\mathbf{M}$, $\mathbf{N}$, and $\mathbf{G}$ are uniquely determined. Therefore, for a given equilibrium, the growth rate of the RT-CD coupled instability is determined solely by the axial perturbation scale kR.

Using the parameters of argon and type I hydrogen jet for $g = 4\times10^{10}\,\mathrm{m/s}^2$, we show in Fig. 2 the instability growth rate as a function of kR (thick solid curve). Also shown are the instability growth rate in the weak gravity limit, strong gravity limit, and zero field limit. For further comparison, Fig. 2 also plots growth rates of the 1D MRT (equivalently, the 2D MRT in undular mode) and the 1D hydrodynamic RT (equivalently, the 2D MRT in interchange mode); the former has $\gamma^2 = gk - v_{Az}^2k^2$ while the latter has $\gamma^2 = gk$.

In both argon and hydrogen jet configurations, very small wavelength perturbations are always suppressed and the peak growth rate occurs at a finite axial wavelength. This is fundamentally different from the 1D hydrodynamic RT instability and the interchange mode of 2D MRT instability.

In the argon plasma jet configuration, $\Phi^2 = 10.0$ and the instability shows strong coupling between RT instability and CD instability. The growth rate of this coupled instability is faster than CD instability because of the effective gravity. At long axial wavelength limit ($kR \to 0$), 1D HD/MHD RT theory gives diminishing growth rate but the RT-CD coupled instability still has large and finite growth rate because RT

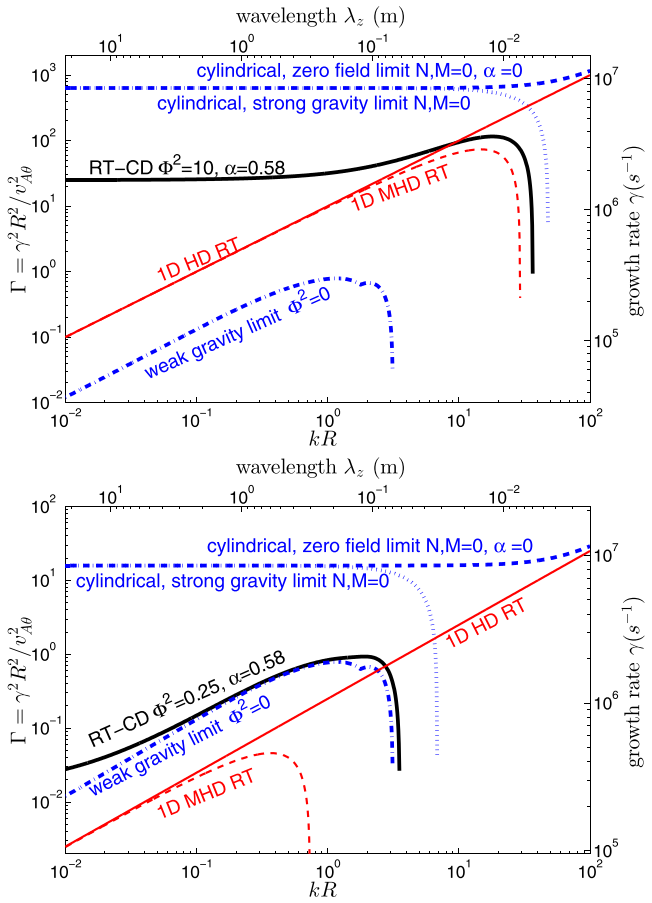

FIG. 2. Instability growth rate as a function of axial perturbation wave number/wavelength for Caltech argon plasma jet with $\Phi^2 = 10$ (top panel) and hydrogen plasma jet with $\Phi^2 = 0.25$ (bottom panel). $\alpha = 0.58$ for both cases. The growth rates are computed using: (1) RT-CD coupled theory for cylindrical plasma (Eq. (47), thick solid curve); (2) weak gravity limit ($\Phi^2 = 0$, Eq. (54), thick dotted-dashed curve); (3) strong gravity limit (**N** and **M** omitted, Eq. (58), thick dotted curve); (4) zero field limit (Eq. (58) with $q = 0$, thick dashed curve); (5) 1D MHD RT theory in axial direction (Eq. (60), light dashed curve); and (6) 1D hydrodynamic RT theory $\gamma^2 = gk$ (light solid curve). The bottom abscissa is the dimensionless variable kR, and the top abscissa gives the dimensioned wavelength $\lambda_z = 2\pi/k$ with $R = 3.5$ cm. The left ordinate is the dimensionless growth rate $\Gamma = \gamma^2 R^2/v_{A\theta}^2$, and the right one is the dimensioned rate γ.

perturbation can develop along the azimuthal direction in the cylindrical interface. On the other hand, the RT-CD instability grows slower than the strong gravity (zero toroidal field) limit or zero field limit, showing the stabilizing effect due to magnetic field B_z and B_θ.

The fastest growth rate of RT-CD instability for argon plasma jet is $\Gamma = 115.6$ at $kR = 18.0$, corresponding to a dimensioned growth rate $\gamma = (v_{A\theta}/R)\sqrt{\Gamma} = 3.6 \times 10^6\,\mathrm{s}^{-1}$ at $\lambda_z = 1.22$ cm. This is very close to the experimental measurement that $\gamma \sim 10^6\,\mathrm{s}^{-1}$ and $\lambda_z \approx 1 - 2$ cm. The 1D MHD RT theory predicts the maximal growth rate as $\Gamma = \Phi^2/(4\alpha^2) = 73.4$ at $kR = \Phi^2/(2\alpha^2) = 14.7$ or $\gamma = 2.9 \times 10^6\,\mathrm{s}^{-1}$ at $\lambda_z = 1.5$ cm. It is seen that the 1D MHD RT theory does provide a reasonable approximation to RT-CD theory, despite the big discrepancy between the two at small kR because of lack of degree of freedom in the azimuthal direction.

The weak gravity limit describes current-driven MHD instabilities such as $m = -1$ kink instabilities. As shown in Fig. 2, the CD instability growth rate of the argon jet is 10–100 times slower than the RT-CD coupled instability. The fastest growth rate in the weak gravity limit is $\gamma = 3 \times 10^5\,\mathrm{s}^{-1}$ at $kR = 1.18$ or $\lambda_z = 18.7$ cm, in excellent agreement with the experimental measurement.[20]

In type I hydrogen jet configuration $\Phi^2 < 1$ due to the low ion mass. Figure 2 confirms that the RT-CD instability in hydrogen jet is essentially reduced to the weak gravity limit. This explains why distinct RT-like ripple is not observed in most hydrogen jet experiments with $g < 10^{11}\,\mathrm{m/s}^2$. The fastest growth rate is $\gamma = 2.1 \times 10^6\,\mathrm{s}^{-1}$ at $\lambda_z = 11.5$ cm. Unlike the argon plasma jet case, the 1D MHD RT theory does not apply to the hydrogen jet system at all.

D. Quasi-paramagnetic property

The classic current-driven instability is paramagnetic in the long wavelength approximation. The surface wavevector $\mathbf{k} = k\hat{z} + m\hat{\theta}/R$ is perpendicular to magnetic field $\mathbf{B} = b_z\hat{z} + b_\theta\hat{\theta}$ on plasma surface, i.e., $\mathbf{k}\cdot\mathbf{B} = kb_z + mb_\theta/R = 0$. This requires a negative m and thus a right handed perturbation. The surface current after perturbation has an additional right handed part, which enhances the equilibrium axial field.[23] The 2D MRT instability allows wavevectors in random direction. However, the interchange mode having wavevector perpendicular to the magnetic field grows fastest because it is not suppressed by the magnetic tension. The interchange mode does not modulate the equilibrium magnetic field. The hydrodynamic 1D Rayleigh-Taylor instability does not involve a magnetic field. In an MHD collimated cylindrical plasma configuration, it is of interest to study the paramagnetic property of RT-CD coupled instability on the curved interface. To see this, we define the spectrum of the fastest eigen-perturbation as

$$f(m) = \frac{|w_m^1|}{\sum_{j\in\mathbb{Z}}|w_j^1|} \qquad m = 0, \pm1, \pm2, \ldots, \tag{62}$$

where $\mathbf{w}^1$ is the eigenvector of $\mathbf{Q}$ corresponding to the largest eigenvalue σ^1. Because $\chi(r = R-) = \sum_m w_m e^{\gamma t + im\theta + ikz}$, $f(m) \sim |w_m^1|$ is the amplitude of the mth azimuthal mode on the plasma surface. We also define the average azimuthal mode number $\bar{m} = \sum_m m f(m)$ and spectral width (standard deviation) $SD = [\sum_m (m - \bar{m})^2 f(m)]^{1/2}$ to quantify how concentrated the spectrum is.

Figure 3 shows the spectra of the fastest growing RT-CD eigen-perturbation of argon and type I hydrogen plasma jet. The spectrum of argon jet reveals a Gaussian profile centered at $\bar{m} = -13.8$ with width $SD = 3.39$, and the hydrogen jet spectrum is sharply centered at $\bar{m} = -1.56$ with $SD = 0.75$. This is consistent with the previous discussion that gravity breaks the axisymmetry and links different m modes together. In a relatively strong gravity case like the argon jet, $\Phi^2 = 10$, gravity is able to create a wide spectrum from $m \approx -23$ to $m \approx -5$. In a weak gravity case like the hydrogen jet, $\Phi^2 = 0.25$, the current-driven instability dominates and gives a sharp spectrum centered between $m = -1$ (kink) and $m = -2$. Figure 3 also demonstrates the validity of truncating the matrix $\mathbf{Q}$ at $p = 70$ because both spectra are essentially zero below $m = -25$ or above $m = 1$.

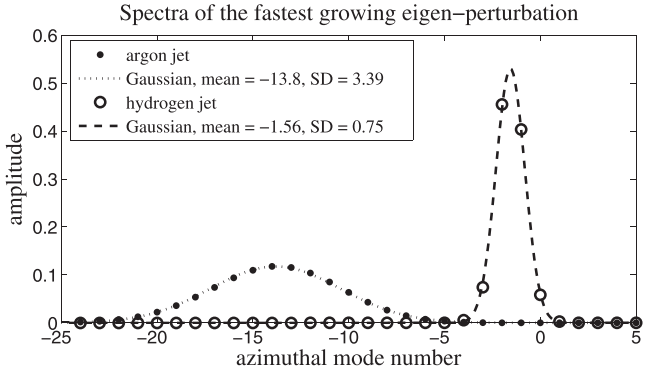

FIG. 3. Spectra of the fastest growing eigen-perturbation for argon jet configuration (solid dots) and hydrogen jet configuration (open circles). The spectrum is defined in Eq. (62). Two Gaussian functions with means and standard deviations calculated using the spectra are also plotted for comparison.

The average mode number $\bar{m}$ is negative for both argon and hydrogen jets so the instability is paramagnetic. The inner product of averaged surface wavevector $\mathbf{k} = k\hat{z} + \bar{m}\hat{\theta}/R$ and magnetic field $\mathbf{B} = b_z\hat{z} + b_\theta\hat{\theta}$ is $\mathbf{k}\cdot\mathbf{B} = k_z b_z + \frac{\bar{m}}{R} b_\theta = b_\theta(q+\bar{m})/R$. Calculation shows that $q = \alpha x = 10.5$ for the argon jet and $q = 1.12$ for the hydrogen jet. For both jets, the safety factor q does not completely cancel $\bar{m}$ so $\mathbf{k}\cdot\mathbf{B} \neq 0$, different from the conventional CD instability or the interchange mode of a 2D MRT instability. Further calculation shows that $\mathbf{k}\cdot\mathbf{B}/|\mathbf{k}||\mathbf{B}| = -0.126$ for the argon jet and -0.154 for the hydrogen jet, giving angles of 97.2° and 98.9° between $\mathbf{k}$ and $\mathbf{B}$ on the plasma surface. We call this property quasi-paramagnetic, because it is slightly different from the paramagnetic behavior of the CD instability. There is a small but finite angle between the magnetic field and the direction of constant instability phase on the plasma surface. This imperfect alignment is a result of the curved interface because on a planar interface the fastest growing modes (interchange modes) always have $\mathbf{k}\cdot\mathbf{B} = 0$.

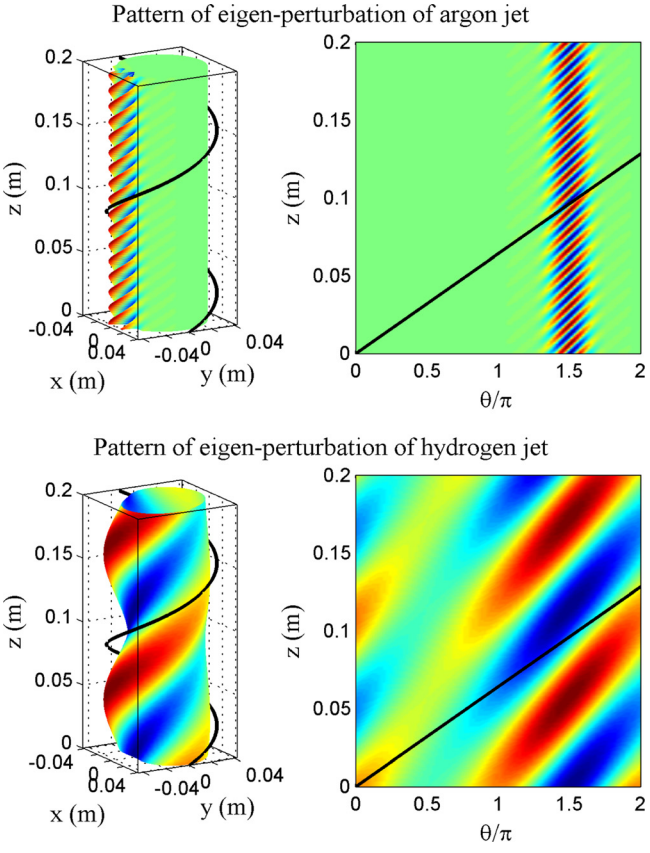

FIG. 4. Pattern of fastest growing eigen-perturbation of argon jet (top) and hydrogen jet (bottom) from $z = 0$ to 0.2 m. The 2D images are $U_{1r}(\theta, z)$ evaluated at plasma surface. The 3D surfaces show the plasma boundary under the fastest growing eigen-perturbation. The black curves illustrate the magnetic field line at the plasma boundary.

E. Visualization of the instability

Figure 4 shows in both 2D and 3D the perturbed surface of argon and type I hydrogen jets given by $U_{1r} \sim \partial\chi/\partial r$

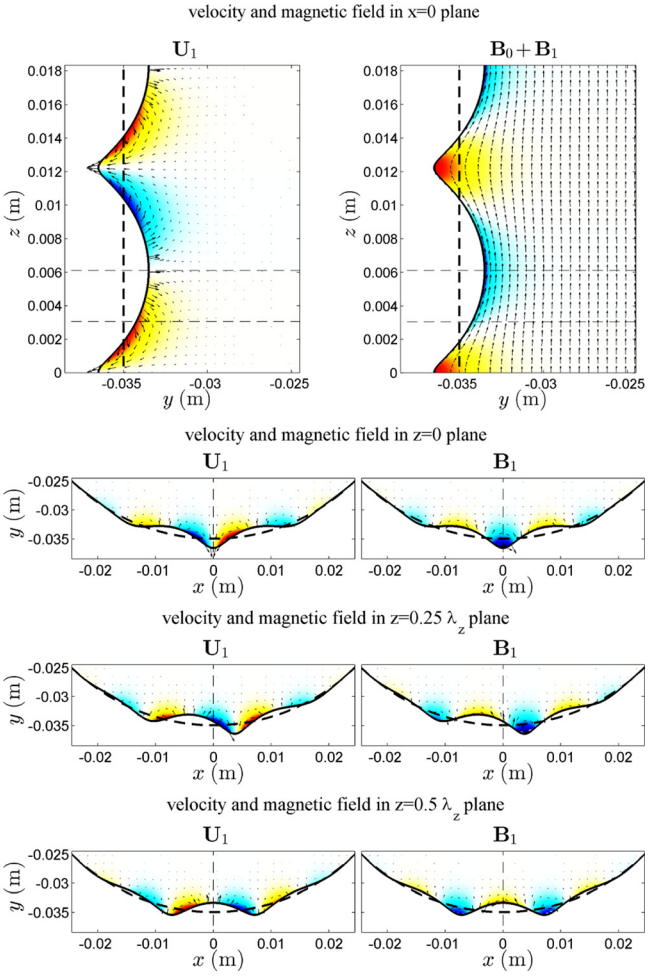

FIG. 5. Velocity and magnetic field of the fastest growing eigen-perturbation of argon jet solution. The top two panels are cross-sectional view on $y - z$ plane at $x = 0$: The background color illustrates azimuthal component ($U_{1\theta}$ or $B_{1\theta}$) and arrows on top represent radial and axial components of $\mathbf{U}_1$ or $\mathbf{B}_0 + \mathbf{B}_1$. The bottom six panels are cross-sectional view on $x - y$ plane at $z = 0$, $z = \lambda_z/4$ and $z = \lambda_z/2$, where $\lambda_z = 1.22$ cm is the axial wavelength of the instability. The locations of these three slices are also marked in the top two panels by thin dashed horizontal lines. In the bottom six panels, the color images are U_{1z} or B_{1z} and arrows represent radial and azimuthal components of $\mathbf{U}_1$ or $\mathbf{B}_1$. The thick dashed lines/curves in each plot are unperturbed surface and the thick solid curves are perturbed surface. Blue/cyan color represents component into the paper and red/yellow color represents component out of the paper. Arrow length is proportional to field strength.

$\sim \sum_m w_m (I'_m/I_m) e^{ikz+im\theta}$. The instability disturbs the argon jet surface primarily around $\theta = 3\pi/2$ because gravity is in the $-\hat{y}$ direction. The instability on the hydrogen jet surface occurs at all θ, because it is a current-driven dominant instability. The gravity nevertheless enhances the perturbation around $\theta = 3\pi/2$ as well. The surface magnetic field (thick black curves) is approximately parallel to the phase of the instability. The argon jet instability shows strong coupling between RT and CD effect. The hydrogen jet case is very similar to a pure $m = -2$ CD instability.

Figure 5 shows the cross-sectional view of velocity and magnetic field under the fastest growing eigen-perturbation inside argon plasma. The figure demonstrates an intrinsic 3D geometry of RT-CD coupled instability. Unstable deformation occurs in both axial and azimuthal direction. The top right panel clearly shows that the poloidal (radial and axial) components of magnetic field remain parallel to plasma surface under perturbation, because of the frozen-in flux requirement. Consequently, the xy-cross-sectional view (bottom six panels) shows amplification in B_z when there is an inward velocity ($U_{1r} < 0$) and vice versa. Finite azimuthal magnetic field is created inside the plasma because of deformation of the surface current.

F. Comprehensive view of RT-CD coupled instability

As this point we have shown two special cases with $\Phi^2 = 0.25$ and $\Phi^2 = 10$ and $\alpha = 0.583$. In general cases, we define $\Gamma(\Phi^2, \alpha, x)$ as the fastest growing solution of Eq. (47) for given Φ^2, α and x, i.e., $\Gamma(\Phi^2, \alpha, x) = \sigma^1 - \alpha^2 x^2$ where σ^1 is the largest eigenvalue of matrix $\mathbf{Q}$.

Now consider a system with Φ^2 and α subject to a random perturbation that contains all possible $x = kR$ components. Those components that give $\Gamma(\Phi^2, \alpha, x) > 0$ are unstable and grow exponentially fast. The component x that gives the largest positive $\Gamma(\Phi^2, \alpha, x)$, denoted as x^*, grows faster than all other components, and is therefore the dominant component. Hence

$$x^*(\Phi, \alpha) = x \text{ that maximizes } \Gamma(\Phi^2, \alpha, x). \tag{63}$$

We further define

$$\Gamma^*(\Phi^2, \alpha) = \max_{x \geq 0} \Gamma(\Phi^2, \alpha, x) = \Gamma(\Phi^2, \alpha, x^*), \tag{64}$$

$$\bar{m}^*(\Phi^2, \alpha) = \bar{m} \text{ of } x^* \text{ eigen–perturbation}, \tag{65}$$

$$SD^*(\Phi^2, \alpha) = SD \text{ of } x^* \text{ eigen–perturbation}. \tag{66}$$

We solve for Γ^*, x^*, $\bar{m}^*$, and SD^* over a wide range of Φ^2 and α and show the results in Fig. 6. The argon jet configuration ($\Phi^2 = 10$, $\alpha = 0.585$) and type I hydrogen jet configuration ($\Phi^2 = 0.25$, $\alpha = 0.583$) are marked in the plots. Also marked is type II hydrogen jet configuration (as "H(2)") with $g = 3 \times 10^{11}$ m/s^2 and so $\Phi^2 = 1.89$. Unlike type I hydrogen jet, this type II hydrogen jet is observed to develop $\lambda_z = 3$–5 cm RT-type ripples in the experiment.

There are two interesting domains in the parameter space that existing theories have already solved.

G. Classic current-driven instability dominated domain

The lower half portion of each plot in Fig. 6 has $\Phi^2 \ll 1$ and is the current-driven instability dominated domain. The impact from gravity is much weaker than that from toroidal field, hence the instability is weakly dependent on Φ^2 in this domain. Type I hydrogen jet experiment is located in this domain (□ symbol). For cases with relatively strong axial field, e.g., $\alpha > 0.6$, the instability occurs with a long axial wavelength (small x^*), and the instability is the standard $m = -1$ kink instability with very sharp spectra. For weak axial field cases (small α), large k and high m modes can develop, but the spectrum remains sharply distributed around the peak

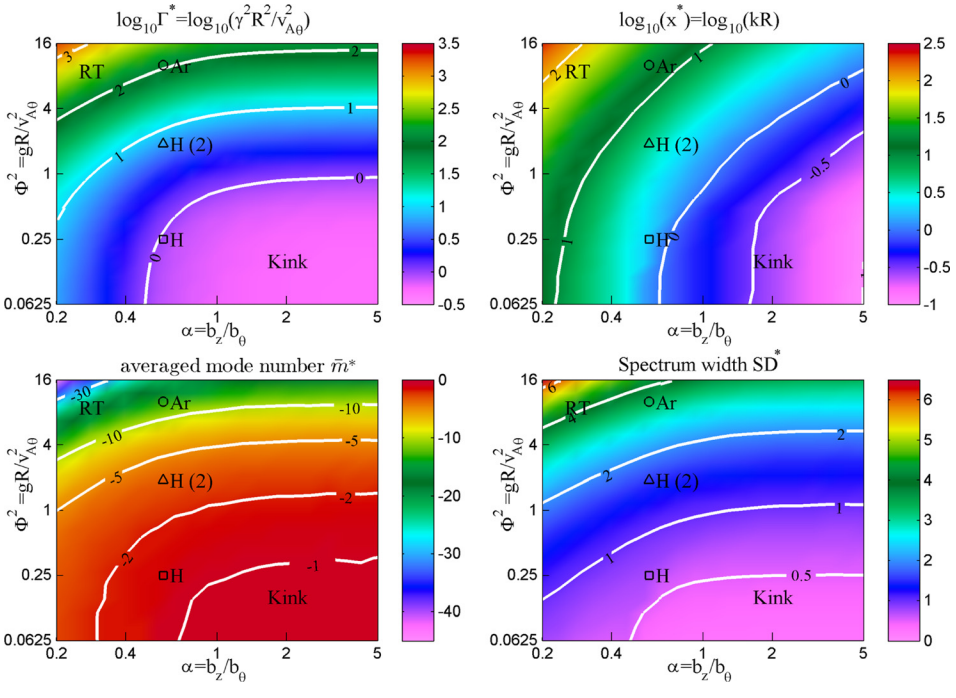

FIG. 6. Solution of $\log_{10}\Gamma^*$ (upper left), $\log_{10}x^*$ (upper right), $\bar{m}^*$ (lower left), and SD^* (lower right) in the $0.0625 \leq \Phi^2 \leq 16$ and $0.2 \leq \alpha \leq 5$ domain. For each (Φ^2, α), we scan x from 10^{-2} to 10^3 and find x^* that maximizes $\Gamma(\Phi^2, \alpha, x)$. The xy axes are both in log scale. Matrix $\mathbf{Q}$ is truncated at $p = 70$ in the calculation. Since $p = 70$ is about 4 times the maximal standard deviation away from the maximal mean mode number ($\max SD^* = 6.5$ and $\max|\bar{m}^*| = 45$), the truncation is valid. The ○ and □ symbols mark the location of argon and type I hydrogen plasma jet configuration with $g = 4 \times 10^{10}$ m/s^2 in the (Φ^2, α) parameter space. The △ symbols mark type II hydrogen configuration with $g = 3 \times 10^{11}$ m/s^2.

mode, because weak gravity cannot efficiently couple different azimuthal modes.

H. Classic Rayleigh-Taylor instability dominated domain

The upper left corner of each subplot (large Φ^2 and small α, or weak B_z and B_θ) is the Rayleigh-Taylor instability dominated domain. The instability occurs with large x^* (small axial wavelength), as well as large and broad azimuthal spectrum (small scaled azimuthal perturbations). These results are consistent with the classic Rayleigh-Taylor instability theory where small scale perturbations have larger growth rates. Equation (61) shows that under the strong gravity limit and short wavelength approximation, the maximum of Γ is obtained at $x^* = \Phi^2/(2\alpha^2)$ as $\Gamma^* = \Phi^4/(4\alpha^2)$. These match with the behaviors of Γ^* and x^* for large Φ^2 and small α. More specifically, in the upper left corner of the subplots, contours of Γ^* have slope $d(\log\Phi^2)/d(\log\alpha) = 1$ and contours of x^* have slope $d(\log\Phi^2)/d(\log\alpha) = 2$, consistent with the 1D MHD RT theory.

Figure 6 shows a continuous transition from $m = -1$ long wavelength kink instability (lower right portion) to 1D hydrodynamic/magnetic Rayleigh-Taylor instability (upper left corner). The argon jet configuration ($\Phi^2 = 10$) and type II hydrogen jet ($\Phi^2 = 1.89$) are located in the transition region. The former case has been discussed in Sec. V C. For the latter case, the theory gives $x^* = 4.3$ or $\lambda_z = 5\,\text{cm}$, consistent with the experiment. In general, when a lateral gravity field is applied to an MHD confined flux rope, the Rayleigh-Taylor and current-driven instability are intrinsically coupled and a unified theory of RT-CD instability on cylindrical geometry should be considered.

VI. SUMMARY AND DISCUSSION

By using linear stability analysis, we have established an analytic theory of a hybrid lateral Rayleigh-Taylor-current-driven coupled instability of an incompressible MHD collimated cylindrical plasma (flux rope) in the presence of a lateral gravitational field. This RT-CD coupled instability is affected by magnetic field tension, curvature, and gravity. The coexistence of lateral gravity and cylindrical geometry leads to a complex coupling of all azimuthal modes of the cylinder, a fundamentally different situation compared to results from a 1D or 2D planar interface. The coupled instability reduces to the classic current-driven instability in the weak gravity limit and to the conventional hydrodynamic or magnetic RT instability in the strong gravity limit. In the general case, the RT and current-driven instabilities are coupled and result in a new hybrid instability.

A useful parameter $\Phi^2 = \mu_0\rho_0 gR/b_\theta^2$ is defined to quantify the relative importance of gravity versus toroidal magnetic field. This parameter is interesting because it includes magnetic field, curvature, plasma density, and gravity, and is completely determined by the equilibrium state. Φ^2 can be written as $\Phi^2 = (\rho_0 gR)/(b_\theta^2/\mu_0)$, which is the ratio of gravitational energy density to toroidal magnetic energy; or it can be written as $\Phi^2 = g/(v_{A\theta}^2/R)$, the ratio between real gravity and effective gravity due to the curvature of the toroidal magnetic field. g is responsible for the RT instability and $v_{A\theta}^2/R$ is responsible for the current-driven instability. Φ^2 describes whether a flux rope is more susceptible to the RT instability (if $\Phi^2 \gg 1$) or the current-driven instability (if $\Phi^2 \ll 1$), or coupled instability ($\Phi^2 \sim 1$).

The RT-CD instability is quasi-paramagnetic since $\bar{m}$ is negative. The instability wavevector $\mathbf{k}$ is nearly perpendicular to the surface magnetic field $\mathbf{B}$ so the instability phase is roughly constant along the magnetic field. Note that on a 2D planar interface $\mathbf{k}\cdot\mathbf{B} = 0$ corresponds to the interchange mode and the instability is essentially identical to the hydrodynamic situation. In cylindrical geometry, the magnetic field prefers a perpendicular $\mathbf{k}$ at the bottom of the flux rope, but as the perturbation extends to other parts of the cylinder, gravity is no longer perpendicular to the interface or can become stabilizing. The combination of magnetic field, cylindrical geometry and gravity can suppress high k modes even when $\mathbf{k}$ is nearly perpendicular to $\mathbf{B}$.

The RT-CD coupled instability theory successfully explains the experimental observation (Fig. 1). For the argon jet, the theory predicts $\lambda_z = 1.22\,\text{cm}$ with growth rate $\gamma = 3.6\times10^6\,\text{s}^{-1}$; for type I hydrogen jet the theory shows that the RT effect is not important and the instability is dominantly current-driven; for type II of hydrogen jet with much larger lateral acceleration, the theory shows RT-CD coupled instability with $\lambda_z \sim 5\,\text{cm}$. Conventional MRT instability theory that only considers axial magnetic field and axial perturbation is able to explain the argon jet, but fails to consider interchange mode or explain hydrogen jets.

Figure 6 shows comprehensive results of RT-CD coupled instability in a large parameter space and illustrates a smooth transition from CD to RT. This figure can be used as function tables for $\gamma^*(\Phi^2,\alpha)$, $x^*(\Phi^2,\alpha)$, $\bar{m}^*(\Phi^2,\alpha)$, and $SD^*(\Phi^2,\alpha)$, because it is difficult to obtain relatively simple explicit functions to approximate the results from the large matrix equations.

This lateral RT-CD coupled instability could be applicable for many situations where there is a flux rope presented in a lateral (effective) gravity. Consider a stationary curved flux rope with minor radius a and major radius b. Assume the axial magnetic field is B_b and azimuthal magnetic field around the plasma axis is B_a (Fig. 7(a)). The curvature of the plasma axis is $1/b$. We define Alfvén speeds $v_{Aa} = B_a/\sqrt{\mu_0\rho}$ and $v_{Ab} = B_b/\sqrt{\mu_0\rho}$. An effective lateral gravity $g_b = v_{Ab}^2/b$ is applied perpendicular to the flux rope axis, pointing in the direction from the curvature center to the flux rope, as indicated by the big arrows in Fig. 7(a). This configuration is analogous to a straight flux rope subject to a lateral gravity as shown in Fig. 7(f). Therefore, the outer surface of the curved flux rope can develop curvature-driven RT instability (Fig. 7(b)). The characteristic parameter Φ^2 in this configuration is $\Phi^2 = g_b/(v_{Aa}^2/a) = aB_b^2/(bB_a^2)$ or $\Phi^2 = B_b/(TB_a) = b/(T^2a)$, where $T = bB_a/(aB_b)$ is a number of twists of the surface helical magnetic field around the axis. If $B_b \sim TB_a$ then a RT-CD coupled instability is expected. If $B_b \ll TB_a$, the flux rope is subject to kink instability (Fig. 7(e)). In the process of flux emergence in the solar corona, a flux rope with a curved axis exists. A typical configuration has $b \sim 2a$ and $T \sim 2$ (e.g., see Ref. 31). Hence $\Phi^2 \sim 0.5$ and $\alpha \sim 1$.

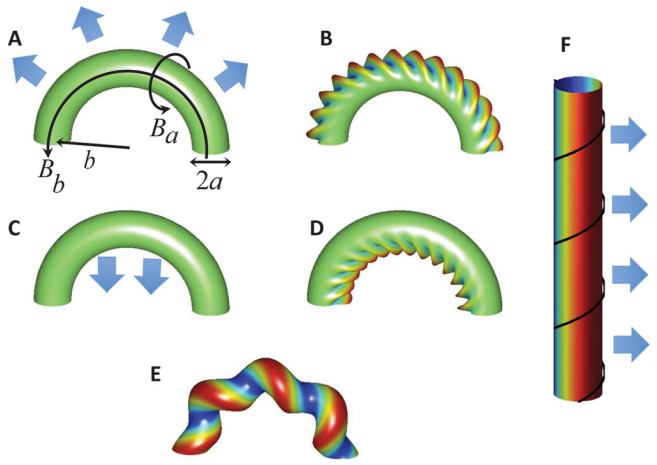

FIG. 7. Configuration of a curved flux rope with minor radius a, major radius b, axial magnetic field B_b, and azimuthal field B_a. Lateral gravity can be caused by magnetic field curvature (panel A), real gravity or lateral acceleration (panel C). Configurations A and C are analogous to a straight flux rope (panel F) with lateral gravity. Flux rope A can develop RT instability similar to panel B and flux rope C can have RT instability similar to panel D. If the gravity effect is weak, the flux rope can undergo kink instability like shown in panel E.

Figure 6 shows that for this configuration the fastest growing mode has $ka = 0.7$ and averaged mode number $\bar{m}^* = -1.2$ with spectrum width $SD^* = 0.75$. Hence, the RT effect is weak and the instability is essentially an $m = -1$ kink instability. In a configuration with larger b and fewer twists, our theory predicts that the RT-CD hybrid instability can develop on the outer edge of the flux ropes. For example, curvature-driven Rayleigh-Taylor instability on the top of solar prominence is studied in theory and is proposed as cause of prominence destabilization and fast magnetic reconnection.[32,33] In Ref. 33, an effective gravity due to the curvature of high-beta prominence $g = V_\parallel^2/R$ is considered, where $V_\parallel$ is the thermal velocity along the magnetic field. The resulted RT instability is also called ballooning instability,[32,33] in analogy to the ballooning mode in magnetic controlled fusion devices. However, in Refs. 32 and 33, concepts of RT and MRT instability of planar interface were used for qualitative or quasi-quantitative analysis. We suggest that the cylindrical geometry is crucial.

Quiescent prominences, believed to be supported by magnetic curvature, can also develop Rayleigh-Taylor instability due to solar gravity.[34] This configuration, illustrated in Fig. 7(c), has curved magnetic fields supporting the structure against gravity, and the equilibrium is susceptible to RT-CD coupled instability at the bottom of the flux rope (Fig. 7(d)). Previous theoretical work by Blokand and Keppens shows that the prominence flux rope under gravity can have instabilities that couple different m modes.[35] 3D numerical simulations have successfully reproduced the fingers/plumes/bubbles structures generated by the RT instability.[36–38] The analytical RT-CD theory presented in this paper is expected to provide more insight into the early phase of these phenomena.

Another potential application is coronal mass ejection (CME), where a flux rope is erupting due to some MHD instability such as the torus instability.[39] As the flux rope is expanding exponentially fast, a lateral effective gravity due to the acceleration is applied on the flux rope pointing opposite to the direction of expansion (Fig. 7(c)). This configuration is very similar to the Caltech plasma jet experiment. A high resolution observation from SDO[40] shows a bright helical brightening with 3–4 turns occurs at 7:24:12 UT below the apex of the prominence of the 2011 Feb 24 CME in active region NOAA 11163. In Ref. 40, this helical brightening is attributed to helical kink instability and is believed to trigger formation of two blobs that later on erupt to give the CME. At 7:30:36 UT some ripple-like fine structures and several helix turns can be seen at inner edge of blob "B." The two blobs accelerated from 100–200 km/s to 600–1000 km/s in about 2 min, resulting in an effective gravity $g \sim 200$–$500\,(\mathrm{km/s})/(\mathrm{min})$ or 3300–8300 m/s^2. This exceeds the solar surface gravity 274 m/s by a factor of 12–30, see Figs. 1 and 4 in Ref. 40 for details. The facts that the helical brightening occurs on the inner edge of the apex of the prominence and the helix turns exist at the inner edge of blob "B" suggest that there could be some RT effect (Fig. 7(d)) coupled in the phenomena. Precise estimation of Φ^2 is not applicable due to lack of detailed measurement, especially of the magnetic field. But a rough estimate gives

$$\Phi^2 = 2.2 \times \left(\frac{g}{500\,\mathrm{km/s/min}}\right) \cdot \left(\frac{n_e}{10^{11}\,\mathrm{cm}^{-3}}\right) \cdot \left(\frac{R}{5\,\mathrm{Mm}}\right) \cdot \left(\frac{20\mathrm{G}}{B_\theta}\right)^2, \tag{67}$$

where the nominal quantities listed in the equation are based on values given in Ref. 40. With these nominal quantities, $\Phi^2 \sim 2$. Therefore, it is likely that the lateral Rayleigh-Taylor-current-driven instability exists. Figure 6 shows that for $\Phi^2 = 2$ and $\alpha = 0.4$, the averaged mode number of the RT-CD instability is $\bar{m}^* \approx -4.5$ with $kR = 10$ and the growth rate is $\gamma^* \approx 13$. This corresponds to an axial perturbation scale $\lambda_z = 2\pi R/(kR) = 0.64R = 3.2\,\mathrm{Mm}$ and growth rate $\gamma = 0.1\,\mathrm{s}^{-1}$ for $n_e = 10^{11}\,\mathrm{cm}^{-3}$, $R = 5\,\mathrm{Mm}$ and $B_\theta = 20$ G. The growth rate is consistent with the life time of the helix turns observed in "blob" B, which is on the order of 20 s. Higher resolution observation is nevertheless necessary to identify whether the phenomena is indeed a RT-CD coupled instability, or just a pure kink. This is because the RT-CD coupled instability is also paramagnetic and could be confused with a current-driven instability. However, if high resolution observation is indeed able to distinguish the two instabilities, it can be used to estimate the magnetic field configuration of the system using the RT-CD theory.

Numerical simulation of buoyant magnetic flux tube in solar convection zone has found a mushroom-shaped RT-type disturbance at bottom of the flux tube,[41,42] and this RT-type disturbance is significantly stabilized by adding more toroidal magnetic field. This is consistent with the RT-CD theory because larger toroidal magnetic field gives smaller Φ^2 and hence the RT effect is weaker. As the flux tube emerges from the convection zone to the solar corona, a filamentary structure can form at the top of the emerging flux tube as a result of MRT instability[43,44] under solar gravity.

The filamentary structure is found to be parallel to the surface magnetic field, consistent with the interchange mode of MRT instability. We suggest that the geometry of the cylindrical emerging flux may also be important and could modulate the behavior of the RT instability. However, we admit that the RT-CD theory presented in this paper should not be directly used in situations such as a buoyant and emerging flux tube, because in these cases the flux tube is surrounded by plasma that can be denser than the flux tube. Nevertheless, the theory suggests that in cylindrical geometry the RT could be fundamentally different from 2D planar case.

ACKNOWLEDGMENTS

We thank Vernon Chaplin for examining the derivation and providing valuable feedback. This work was supported by the U.S. Department of Energy Office of Science, Office of Fusion Energy Sciences under Award Nos. DE-FG02-04ER54755 and DE-SC0010471, by the National Science Foundation under Award No. 1059519, and by the Air Force Office of Scientific Research under Award No. FA9550-11-1-0184.

APPENDIX A: EQUILIBRIUM SOLUTION

In this section, we consider two scenarios that can accelerate the plasma tube in lab frame, or equivalently support the plasma against gravity in the frame of plasma. The first scenario includes the hoop force $J_z B_x$ term in Eq. (6) and the second scenario considers the magnetic buoyancy $J_x B_z$ term in Eq. (6).

1. Hoop force scenario

In the experiment, the acceleration of the kink is caused by the hoop force. Consider each part of the kink as a half torus. The flux surfaces at the cross-section of the torus are not perfectly concentric circles but are instead more dense inside than outside. Therefore, the kinked plasma tube has stronger B_θ at lower y and weaker B_θ at larger y. In a straight plasma tube configuration, such a non-concentric B_θ can be considered as an azimuthally symmetric $B_{0\theta}$ and an additional horizontal field B_x. B_x enhances B_θ at lower y and reduces it at upper y. In a simple configuration, we assume the equilibrium magnetic field profile is

$$\mathbf{B}_0 = b_z\hat{z} + b_\theta \frac{R}{r} H(r-R)\hat{\theta} + b_x\hat{x}, \tag{A1}$$

where b_z, b_θ, and b_x are all constant. Hence, $\mathbf{J}_0 = J_{0z}\hat{z}$ and $J_{0z} = b_\theta R/(\mu_0 r)\delta(r-R)$ only exists on plasma surface. The Lorentz force

$$\mathbf{J}_0 \times \mathbf{B}_0 = -J_{0z}B_{0\theta}\hat{r} + J_{0z}b_x\hat{y} \tag{A2}$$

has a radial component which confines the plasma tube and a vertical component which is the hoop force. In the lab frame, the hoop force expands the kinked plasma. In the frame of plasma tube, the hoop force supports the tube against the gravity.

In equilibrium, $\mathbf{U}_0 = 0$ and so Eqs. (3)–(5) reduce to

$$-\nabla P_0 + \mathbf{J}_0 \times \mathbf{B}_0 - \rho g\hat{y} = 0. \tag{A3}$$

Inside the plasma tube, $\rho = \rho_p$ is constant and $\mathbf{J}_0 = 0$. Hence the equilibrium is simply

$$P_0(y) = P_0(0) - \rho_p g y, \quad r < R, \tag{A4}$$

where $P_0(0)$ is the plasma pressure at $y = 0$. The radial component of Eq. (A3) upon substitution of Eq. (A2) is

$$-\frac{\partial P_0}{\partial r} - \frac{b_\theta^2 R^2}{\mu_0 r^2}\delta(r-R)H(r-R) + \frac{b_\theta b_x R}{\mu_0 r}\delta(r-R)\sin\theta - \rho g\sin\theta = 0. \tag{A5}$$

Integrate Eq. (A5) from $r = R-$ to $r = R+$ and use Eq. (A4) and $P_0(R+) = 0$ to obtain

$$P_0(0) - \rho_p g R\sin\theta - \frac{b_\theta^2}{2\mu_0} + \frac{b_\theta b_x}{\mu_0}\sin\theta = 0. \tag{A6}$$

Eq. (A6) should hold for all θ and so

$$P_0(0) = \frac{b_\theta^2}{2\mu_0} = \frac{\mu_0 I_0^2}{8\pi^2 R^2}, \quad \rho_p g R = \frac{b_\theta b_x}{\mu_0}, \tag{A7}$$

where I_0 is the total axial current. Hence b_θ or axial current is responsible for confining the plasma tube and b_x or hoop force is responsible for balancing the gravity. Although the $J_z B_x$ force is only applied to the surface of the plasma, the incompressible plasma is able to distribute the Lorentz force to region $r < R$ via Eq. (A4). Note that b_θ and b_x have the same sign therefore $B_\theta(x=0, y=-R) = b_\theta + b_x > B_\theta(x=0, y=R) = b_\theta - b_x$, consistent with the previous analysis. The equilibrium solution is similar to a typical Z-pinch configuration except that $P_0(y)$ is y-dependent because of gravity.

In typical Caltech plasma jet experiments, the axial current is $I_z = 50$–$150\,\mathrm{kA}$. The nominal jet radius $R \sim 2\,\mathrm{cm}$, then b_θ is on the order of 1 T. The plasma number density is estimated around $n_e = 10^{21} \sim 10^{22}\,\mathrm{m}^{-3}$. With $g \sim 10^{10}\,\mathrm{m/s}^2$, hydrogen jet requires $b_x = 4\times10^{-5}$–$4\times10^{-4}\,\mathrm{T} \ll b_\theta$ and argon jet requires $b_x = 0.017$–$0.17\,\mathrm{T} \ll b_\theta$. For some hydrogen jet experiments with $g \sim 10^{11}\,\mathrm{m/s}^2$, $b_x \ll b_\theta$ is still valid. This means that a small b_x component is sufficient to provide the acceleration. In such a case, we can make a zero order approximation $b_x \simeq 0$ so that the equilibrium magnetic configuration is as in Eq. (7).

2. Magnetic buoyancy scenario

Another mechanism that can support the plasma tube is magnetic buoyancy. In the original theory of MHD RT instability occurring on a planar interface by Kruskal and Schwarzschild,[4] two uniform magnetic fields parallel to the interface but with different strength were used to provide a magnetic pressure difference across the interface to support a plasma above vacuum. In the cylindrical case, instead of assuming an abrupt change across the interface, we assume

that in equilibrium the axial magnetic field has a small component that varies in the y direction in addition to a uniform field b_z, i.e.,

$$B_{0z}(y) = b_z + \tilde{b}_z(y). \tag{A8}$$

Without loss of generality, we assume $\tilde{b}_z(y=0)=0$ so that $B_{0z}(y=0)=b_z$. $\tilde{b}_z(y=0)$ requires $J_x = \partial_y \tilde{b}_z(y)/\mu_0$ in both the plasma and the surrounding medium. Therefore, the background is not a pure vacuum, but a low-density plasma that has negligible pressure compared to the central plasma tube and is able to conduct current to allow $\tilde{b}_z(y)$. Assume the toroidal magnetic field as

$$B_{0\theta} = \frac{b_\theta R}{r} H(r-R), \tag{A9}$$

and there is no other magnetic field component.

In equilibrium the MHD momentum equation (4) becomes

$$0 = \frac{1}{\mu_0}\mathbf{B}_0 \cdot \nabla \mathbf{B}_0 - \nabla\left(P + \frac{B_0^2}{2\mu_0}\right) - \rho g \hat{y}. \tag{A10}$$

It is seen that

$$\begin{aligned}\mathbf{B}_0 \cdot \nabla \mathbf{B}_0 &= (B_{0z}\hat{z} + B_{0\theta}\hat{\theta}) \cdot \nabla (B_{0z}(y)\hat{z} + B_{0\theta}(r)\hat{\theta}),\\ &= B_{0\theta}\frac{1}{r}\frac{\partial B_{0z}(y)}{\partial \theta}\hat{z} + B_{0\theta}^2 \hat{\theta}\cdot\nabla\hat{\theta},\\ &= \frac{B_{0\theta}}{r}\frac{\partial \tilde{b}_z(y)}{\partial \theta}\hat{z} - \frac{B_{0\theta}^2}{r}\hat{r}.\end{aligned} \tag{A11}$$

Inside the plasma tube, $\mathbf{B}_0 \cdot \nabla \mathbf{B}_0 = 0$ because $B_{0\theta}=0$. Assuming constant plasma density $\rho = \rho_p$ for $r<R$ so that Eq. (A10) can be written as

$$-\nabla\left(P + \frac{B_0^2}{2\mu_0} + \rho_p g y\right) = 0 \qquad r<R. \tag{A12}$$

The equilibrium inside the plasma tube is therefore

$$P(y) + \frac{B_{0z}(y)^2}{2\mu_0} + \rho_p g y = const = P(0) + \frac{B_{0z}(0)^2}{2\mu_0}, \quad r<R. \tag{A13}$$

Now consider integration of Eq. (A10) across the interface. Because the first and last terms on the right hand side of Eq. (A10) do not contain any delta-function-like component, integration of Eq. (A10) from $r=R-$ to $r=R+$ gives

$$\left(P + \frac{B_0^2}{2\mu_0}\right)_{R-} = \left(P + \frac{B_0^2}{2\mu_0}\right)_{R+}, \tag{A14}$$

so

$$\begin{aligned}&P(y) + \frac{B_{0z}(y)^2}{2\mu_0} = \frac{B_{0z}(y)^2}{2\mu_0} + \frac{B_{0\theta}(R+)^2}{2\mu_0}\\ &\Rightarrow \quad P(y) = \frac{B_{0\theta}(R+)^2}{2\mu_0} = \frac{b_\theta^2}{2\mu_0},\end{aligned} \tag{A15}$$

i.e., pressure inside the plasma tube is uniform and equals to the toroidal magnetic pressure at the tube boundary, identical to the classic Bennett Z-pinch configuration. We substitute $P(y)=P(0)$ into Eq. (A13) and use Eq. (A8) to get

$$\frac{(b_z + \tilde{b}_z)^2}{2\mu_0} + \rho_p g y = \frac{b_z^2}{2\mu_0}. \tag{A16}$$

B_{0z} is stronger at lower y and weaker at higher y so that the magnetic pressure gradient is in the $+y$ direction to support the plasma tube against gravity $-g\hat{y}$. Eq. (A16) becomes

$$\tilde{b}_z(y) b_z + \mu_0 \rho g y \simeq 0, \tag{A17}$$

assuming $|\tilde{b}_z| \ll |b_z|$. This gives

$$\tilde{b}_z(y) \simeq -\frac{\mu_0 \rho g y}{b_z}. \tag{A18}$$

In typical Caltech plasma jet experiments, the axial magnetic field strength is around $B_z \sim 0.6$ T (e.g., see Fig. 6 in Ref. 19) and $n_e = 10^{21} - 10^{22}\,\mathrm{m}^{-3}$. With a jet radius $R \sim 2$ cm and $g \sim 10^{10}\,\mathrm{m/s}^2$, hydrogen jet has

$$\frac{|\tilde{b}_z|}{|b_z|} \simeq \frac{\mu_0 n_e m_H g R}{B_z^2} \approx 10^{-3}\text{–}10^{-2},$$

and argon jet has

$$\frac{|\tilde{b}_z|}{|b_z|} \simeq \frac{\mu_0 n_e m_{Ar} g R}{B_z^2} \approx 0.04\text{–}0.4.$$

For some rare hydrogen experiments with $g \sim 10^{11}\,\mathrm{m/s}^2$, $\mu_0 \rho_p g R/B_z^2 \sim 6\times 10^{-2} \ll 1$ is also valid.

Therefore, in most cases it is safe to assume that the axial field b_z is significantly larger than the y-dependent component $\tilde{b}_z(y)$, i.e., a small B_{0z} variation in the y direction is sufficient to provide enough magnetic buoyancy to support the central plasma tube. In such a case, we make a zero order approximation $\tilde{b}_z(y) \simeq 0$ so that the equilibrium magnetic field configuration is as described in Eq. (7).

The magnetic buoyancy scenario requires that the surrounding medium is a low-density, low-pressure plasma. However, because magnetic buoyancy also exists in the background, there is no equilibrium outside the plasma tube. Instead, the background is a thin accelerating wind as seen by the plasma tube. This does not affect the instability derivation as long as the background medium has negligible density and pressure compared to the plasma tube.

Among the two scenarios, the hoop force scenario is likely to be the dominant one in the experiment. One evidence is that in some argon cases the quantity $\mu_0 \rho_p g R/B_z^2$ may be comparable to or even greater than unity, showing that the magnetic buoyancy solely due to B_z is not sufficient. In both scenarios, we obtain the same azimuthally symmetric magnetic field configuration as described in Eq. (7) after some approximation. Sophisticated numerical simulation is required in order to accurately model the equilibrium and instability. In this paper, we consider simple but non-trivial solutions that can analytically exhibit coupling between

Rayleigh-Taylor and current-driven instability. Hence, we still use the simple configuration Eq. (7) in our solution while acknowledging that the solution is based on an approximate equilibrium.

APPENDIX B: CONFINED PERTURBED CURRENT

Inside the plasma, $\rho_1 = 0$ and $\mathbf{B}_0 = b_z\hat{z}$ so the momentum equation (11) becomes

$$\gamma\rho_p\mathbf{U}_1 = -\nabla\left(P_1 + \frac{\mathbf{B}_0\cdot\mathbf{B}_1}{\mu_0}\right) + \frac{ikb_z}{\mu_0}\mathbf{B}_1. \tag{B1}$$

Use Eq. (29) to eliminate $\mathbf{U}_1$ in Eq. (B1) and get

$$\frac{\gamma^2\rho_p}{ikb_z}\mathbf{B}_1 = -\nabla\left(P_1 + \frac{\mathbf{B}_0\cdot\mathbf{B}_1}{\mu_0}\right) + \frac{ikb_z}{\mu_0}\mathbf{B}_1. \tag{B2}$$

The curl of this equation gives

$$-i\left(\frac{\gamma^2\rho_p}{kb_z} + \frac{kb_z}{\mu_0}\right)\nabla\times\mathbf{B}_1 = 0. \tag{B3}$$

For an instability $\gamma^2 > 0$ and so $\gamma^2\rho_0/ikb_z - ikb_z/\mu_0 \neq 0$. Therefore, $\mu_0\mathbf{J}_1 = \nabla\times\mathbf{B}_1 = 0$ inside plasma and $\mathbf{J}_1$ is confined in the interface.

[1]D. H. Sharp, Phys. D **12**, 3 (1984).
[2]P. M. Bellan, *Fundamentals of Plasma Physics* (Cambridge University Press, 2006).
[3]S. Chandrasekhar, *Hydrodynamic and Hydromagnetic Stability* (Clarendon Press, Oxford, 1961).
[4]M. D. Kruskal and M. Schwarzschild, Proc. R. Soc. London, Ser. A **223**, 348 (1954).
[5]J. M. Stone and T. Gardiner, Astrophys. J. **671**, 1726 (2007).
[6]E. G. Harris, Phys. Fluids **5**, 1057 (1962).
[7]D. L. Peterson, R. L. Bowers, J. H. Brownell, A. E. Greene, K. D. McLenithan, T. A. Oliphant, N. F. Roderick, and A. J. Scannapieco, Phys. Plasmas **3**, 368 (1996).
[8]M. K. Matzen, Phys. Plasmas **4**, 1519 (1997).
[9]X. M. Qiu, L. Huang, and G. D. Jian, Phys. Plasmas **10**, 2956 (2003).
[10]H. Takabe, K. Mima, L. Montierth, and R. L. Morse, Phys. Fluids **28**, 3676 (1985).
[11]R. Betti, V. N. Goncharov, R. L. McCrory, and C. P. Verdon, Phys. Plasmas **5**, 1446 (1998).
[12]E. N. Parker, Astrophys. J. **145**, 811 (1966).
[13]D. J. Acheson, Sol. Phys. **62**, 23 (1979).
[14]D. W. Hughes and F. Cattaneo, Geophys. Astrophys. Fluid Dyn. **39**, 65 (1987).
[15]J. Kim, D. Ryu, S. Hong, S. Lee, and J. Franco, in *How does the Galaxy Work?*, Astrophysics and Space Science Library, edited by E. J. Alfaro, E. Pérez, and J. Franco (Springer Netherlands, 2005), Vol. 315, pp. 315–322.
[16]D. Dobrott, D. B. Nelson, J. M. Greene, A. H. Glasser, M. S. Chance, and E. A. Frieman, Phys. Rev. Lett. **39**, 943 (1977).
[17]J. Wesson, *Tokamak* (Oxford University Press, 1987).
[18]E. Hameiri, P. Laurence, and M. Mond, J. Geophys. Res. **96**, 1513, doi:10.1029/90JA02100 (1991).
[19]X. Zhai, H. Li, P. M. Bellan, and S. Li, Astrophys. J. **791**, 40 (2014).
[20]A. L. Moser and P. M. Bellan, Nature **482**, 379 (2012).
[21]G. S. Yun and P. M. Bellan, Phys. Plasmas **17**, 062108 (2010).
[22]D. Kumar and P. M. Bellan, Phys. Rev. Lett. **103**, 105003 (2009).
[23]S. C. Hsu and P. M. Bellan, Phys. Rev. Lett. **90**, 215002 (2003).
[24]K. Chai, X. Zhai, and P. M. Bellan, Phys. Plasmas **23**, 032122 (2016).
[25]R. C. Kerr and J. R. Lister, Earth Planet. Sci. Lett. **88**, 143 (1988).
[26]J. R. Lister and R. C. Kerr, J. Fluid Mech. **202**, 577 (1989).
[27]J. R. Lister, R. C. Kerr, N. J. Russell, and A. Crosby, J. Fluid Mech. **671**, 313 (2011).
[28]J. P. Freidberg, *Ideal Magnetohydrodynamics* (Plenum Press, New York, 1987).
[29]M. Abramowitz and I. A. Stegun, *Handbook of Mathematical Functions: With Formulas, Graphs, and Mathematical Tables* (Dover Publications, New York, 1964).
[30]S. Noschese, L. Pasquini, and L. Reichel, Numer. Linear Algebra Appl. **20**, 302 (2013).
[31]S. E. Gibson, Y. Fan, C. Mandrini, G. Fisher, and P. Demoulin, Astrophys. J. **617**, 600 (2004).
[32]L. A. Pustil'nik, Sov. Astron. **17**, 763 (1973).
[33]K. Shibasaki, Astrophys. J. **557**, 326 (2001).
[34]T. Berger, P. Testa, A. Hillier, P. Boerner, B. C. Low, K. Shibata, C. Schrijver, T. Tarbell, and A. Title, Nature **472**, 197 (2011).
[35]J. W. S. Blokand and R. Keppens, Astron. Astrophys. **532**, A94 (2011).
[36]A. Hillier, H. Isobe, K. Shibata, and T. Berger, Astrophys. J. Lett. **736**, L1 (2011).
[37]J. Terradas, R. Soler, M. Luna, R. Oliver, and J. L. Ballester, Astrophys. J. **799**, 94 (2015).
[38]R. Keppens, C. Xia, and O. Porth, Astrophys. J., Lett. **806**, L13 (2015).
[39]B. Kliem and T. Török, Phys. Rev. Lett. **96**, 255002 (2006).
[40]P. Kumar, K.-S. Cho, S.-C. Bong, S.-H. Park, and Y. H. Kim, Astrophys. J. **746**, 67 (2012).
[41]S. B. F. Dorch and A. Nordlund, Astron. Astrophys. **338**, 329 (1998).
[42]S. B. F. Dorch, V. Archontis, and A. Nordlund, Astron. Astrophys. **352**, L79 (1999).
[43]H. Isobe, T. Miyagoshi, K. Shibata, and T. Yokoyama, Nature **434**, 478 (2005).
[44]H. Isobe, T. Miyagoshi, K. Shibata, and T. Yokoyama, Publ. Astron. Soc. Jpn. **58**, 423 (2006).